

Manuscript Number:

Title: The out-of-plane compressive response of Dyneema composites

Article Type: Research Paper

Corresponding Author: Dr. Vikram Deshpande,

Corresponding Author's Institution:

First Author: J Attwood

Order of Authors: J Attwood; S Khaderi; K Karthikeyan; N Fleck; M O'Masta; H Wadley; Vikram Deshpande

Abstract: Out-of-plane compression tests were conducted on six grades of ultra high molecular weight polyethylene fibre composites (Dyneema) with varying grades of fibre and matrix, ply thickness, and ply stacking sequence. The composites with a [0/90] lay-up had an out-of-plane compressive strength that was dictated by in-plane tensile fibre fracture. By contrast, the out-of-plane compressive strength of the uni-directional composites was significantly lower and was not associated with fibre fracture. The peak strength of the [0/90] composites increased with increasing in-plane specimen dimensions and was dependent on the matrix and fibre strength as well as on the ply thickness. A combination of micro X-ray tomography and local pressure measurements revealed the existence of a shear-lag zone at the periphery of the specimens. Finite Element (FE) and analytical micromechanical models predict the compressive composite response and reveal that out-of-plane compression generates tensile stresses along the fibres due to shear-lag loading between the alternating 0 and 90 plies. Moreover, the compressive strength data suggests that the shear strength of Dyneema is pressure sensitive, and this pressure sensitivity is quantified by comparing predictions with experimental measurements of the out-of-plane compressive strength. Both the FE and analytical models accurately predict the sensitivity of the compressive response of Dyneema to material and geometric parameters: matrix strength, fibre strength and ply thickness.

Suggested Reviewers:

Opposed Reviewers:

The out-of-plane compressive response of Dyneema[®] composites

J.P. Attwood^a, S.N. Khaderi^a, Karthikeyan K.^a, N.A. Fleck^a, M.R. O'Masta^b, H.N.G. Wadley^b, V.S. Deshpande^{a,*}

^a*Department of Engineering, Cambridge University, Trumpington Street, Cambridge CB2 1PZ, UK*

^b*Department of Materials Science & Engineering, School of Engineering and Applied Science, University of Virginia, Charlottesville, VA 22904, USA.*

Abstract

Out-of-plane compression tests were conducted on six grades of ultra high molecular weight polyethylene fibre composites (Dyneema[®]) with varying grades of fibre and matrix, ply thickness, and ply stacking sequence. The composites with a $[0^\circ/90^\circ]$ lay-up had an out-of-plane compressive strength that was dictated by in-plane tensile fibre fracture. By contrast, the out-of-plane compressive strength of the uni-directional composites was significantly lower and was not associated with fibre fracture. The peak strength of the $[0^\circ/90^\circ]$ composites increased with increasing in-plane specimen dimensions and was dependent on the matrix and fibre strength as well as on the ply thickness. A combination of micro X-ray tomography and local pressure measurements revealed the existence of a shear-lag zone at the periphery of the specimens. Finite Element (FE) and analytical micromechanical models predict the compressive composite response and reveal that out-of-plane compression generates tensile stresses along the fibres due to shear-lag loading between the alternating 0° and 90° plies. Moreover, the compressive strength data suggests that the shear strength of Dyneema[®] is pressure sensitive, and this pressure sensitivity is quantified by comparing predictions with experimental measurements of the out-of-plane compressive strength. Both the FE and analytical models accurately predict the sensitivity of the compressive response of Dyneema[®] to material and geometric parameters: matrix strength, fibre strength and ply thickness.

Keywords: Pressure dependent shear strength, shear lag, composites.

*Corresponding author *E-mail address:* vsd@eng.cam.ac.uk

1. Introduction

Low density fibre composites are increasingly used in lightweight structures where ballistic resistance is a requirement. Kevlar, other aramid composites, and more recently composites made from ultra high molecular weight polyethylene (UHMWPE) fibres embedded in thermoplastic matrices, are exploited for their superior impact resistance.

Ultra high molecular weight polyethylene fibres were commercialised in the late 1970s by DSM Dyneema, NL under the trade name Dyneema[®], and more recently by Honeywell in the USA under the name Spectra[®]. A number of studies have been conducted to measure the static stress-strain response (Liu et al., 2014; Wilding and Ward, 1978; Govaert and Lenstra, 1992) and dynamic stress-strain response (Russell et al., 2013; O’Masta et al., 2013; Koh et al., 2010; Benloulou et al., 1997) of UHMWPE fibres and their composites. For example, Russell et al. (2013) have observed that UHMWPE composites have tensile strengths of a few GPa but shear strengths of only a few MPa. Moreover, they found that the tensile strength of UHMWPE fibres displays nearly no strain rate dependence for strain rates up to 10^3s^{-1} . Such measurements have been utilized for the development of continuum models (Grujicic et al., 2009; Iannucci and Pope, 2011) with the goal of predicting the penetration resistance of UHMWPE composites. However, penetration calculations performed using such constitutive models (Grujicic et al., 2009; Iannucci and Pope, 2011) are typically unable to predict the ballistic performance of UHMWPE composites unless unrealistic material parameters are employed (for example, a tensile strength of 6 GPa is used in these numerical models rather than the measured value of approximately 2 GPa).

An alternative approach to predicting the ballistic performance of UHMWPE composites is based on the scaling relation of Cunniff (1999). He argued that the ballistic limit of fibre composites scales linearly with the so-called Cunniff parameter

$$c^* = \left(\frac{s_f e_f}{2\rho_f} \sqrt{\frac{Y_f}{\rho_f}} \right)^{1/3} \quad (1)$$

where s_f and e_f are the tensile failure strength and failure strain of the fibres respectively, and Y_f is the tensile modulus of the fibres, of density ρ_f . In an elegant analytical study, Phoenix and Porwal (2003) demonstrated that the ballistic limit of composite plates scales with c^* when an impacted plate

undergoes membrane stretching deformation and failure. However, there is growing experimental evidence that the matrix shear strength (which governs the inter-laminar shear strength) has a significant influence on the ballistic performance of UHMWPE composites. For example, Karthikeyan et al. (2013b) have reported ballistic measurements where the composite shear strength was systematically varied, while keeping the tensile strength in the fibre directions fixed. Their measurements show a clear trend whereby the ballistic resistance increases with decreasing shear strength; such an effect is neither captured by the scaling relation (1), nor predictable from a membrane stretching analysis. Further, Greenhalgh et al. (2013) have reported a detailed fractography study and argued qualitatively that the matrix shear strength influences energy absorption and failure mechanisms such as delamination and splitting.

UHMWPE composites are often loaded in out-of-plane compression. For example, the normal impact of projectiles against UHMWPE composites during ballistic events generates out-of-plane compressive loading beneath the projectile. Similarly, the clamping pressure to grip a composite plate results in out-of-plane compressive loading with rather surprising consequences to the structural response, as detailed below.

1.1. Effect of clamping on the failure of Dyneema[®] beams

Our interest in the out-of-plane compressive response of composites originated during experiments by Karthikeyan et al. (2013a), on the stretch-bend response of clamped Dyneema[®] beams (grade HB50) using the apparatus sketched in Fig. 1. Beams of length 400 mm, width 35 mm and thickness 6 mm were clamped by 5 M6 bolts and a 10 mm thick steel cover plate at each end, as sketched in Fig. 1a(i). The free-span of the beams was 200 mm and the bolts were tightened to a torque of 9 Nm. The measured load F versus central roller displacement δ from the study of Karthikeyan et al. (2013a) is given in Fig. 1b, and a photograph of the observed failure mode of the HB50 beams is shown in Fig. 1c. In-plane failure of the Dyneema[®] occurred between the bolt-holes within the clamped region; fibre fracture occurred with minimal deformation of the bolt-holes. The measured load versus displacement curve exhibited a dramatic load drop at the point of fibre failure.

Here we repeated the stretch-bend test of Karthikeyan et al. (2013a) with one small modification. A spacer was introduced into the clamping set-up such that the steel cover no longer applied a clamping pressure; see Fig. 1a(ii).

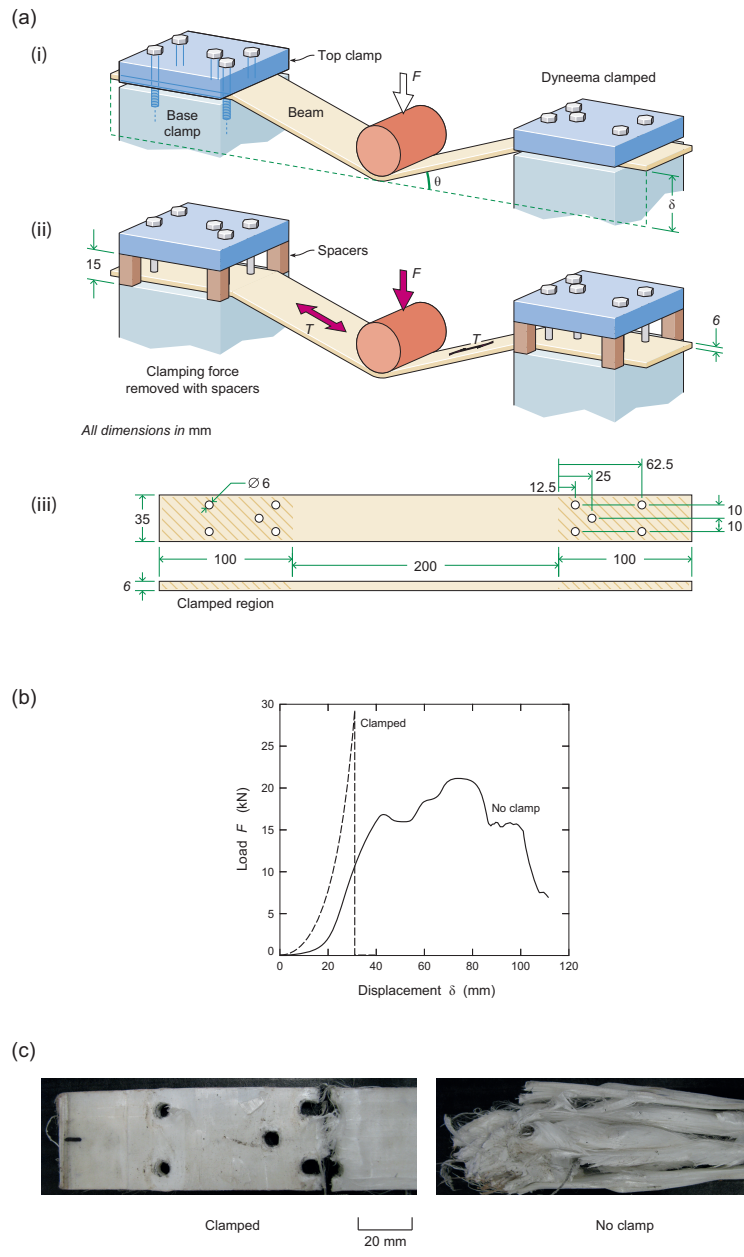


Figure 1: (a) Sketch of the 3-point bending set-up for HB50 Dyneema[®] beams. The three sub-parts show (i) the reference setup where the grips apply clamping pressure; (ii) the modification with of the grips so as to not apply clamping pressure and (iii) the arrangement of the bolt holes. (b) The measured applied load F versus displacement δ response of the HB50 beams with and without the grip clamping pressure. (c) Photographs of the failed ends of the beams which illustrate the dramatic difference in the failure mode between the two end clamping conditions.

The measured load versus displacement curve for the case with no clamping pressure has been added to Fig. 1b and a photograph of the section of the beam within the clamping zone at a displacement $\delta = 115\text{mm}$ is included in Fig. 1c. There is a dramatic change in failure mode, due to relaxation of the clamping constraint. Extensive in-plane shear deformation now occurs and this results in elongation of the bolt-holes, with no fibre fracture. Consequently, the load versus displacement curve shows no dramatic load drop.

These observations suggest that the shear strength of the HB50 Dyneema[®] composite is *pressure sensitive*. This is consistent with a large body of data on polymers including polyethylene, see for example Ward (1971). When clamping pressure is applied the shear strength is enhanced such that it allows the net-section stress within the beam to build up to the fibre failure stress. In contrast, when no clamping pressure is applied the low shear strength of the HB50 composite resulted in shear deformation at the sides of the bolts, and the net section stress does not attain the level required to cause fibre fracture. We conclude that constraint has a major effect on the observed failure mechanism.

A literature search reveals that little is known about the out-of-plane response of fibre composites. Henriksson (1990) presented an elastic laminate plate theory analysis to calculate the out-of-plane modulus of cross-play CFRP composites but no analysis of the plastic response and associated failure were given. To-date there have been no investigations of the out-of-plane compressive behaviour of Dyneema[®] composites and any associated pressure sensitivity of the shear strength. This is the focus of the present study.

The outline of the paper is as follows. First, we summarise the manufacturing process of DSM Dyneema, NL followed by a description of the microstructure and composition for several grades of Dyneema[®]. Second, the in-plane tensile response and inter-laminar shear response of these composites are reported. The sensitivity of the out-of-plane compressive response of Dyneema[®] composites to the inter-laminar shear strength, the fibre strength, ply stacking sequence and ply thickness are determined. Finally, we describe analytical and finite element (FE) models for the out-of-plane compressive response and validate the predictions by the measurements.

2. Composite manufacture and configurations

Six grades of Dyneema[®] composites were investigated in this study: five of these grades were composites with a $[0^\circ/90^\circ]$ stacking sequence and manufactured by DSM, while a sixth grade comprised unidirectional plies that were stacked in-house. The manufacturing steps employed by DSM, to construct composites with the $[0^\circ/90^\circ]$ stacking sequence and a polyurethane matrix, were detailed in Russell et al. (2013). These steps are applicable to all $[0^\circ/90^\circ]$ grades discussed here, with minor alterations according to the matrix material used.

- I: Fibres are produced through a gel-spinning/hot drawing process (Smith et al., 1979; Smith and Lemstra, 1980). The UHMWPE is dissolved in a solvent at a temperature of 150°C and the solution is pumped through a spinneret comprising a few hundred capillaries to form liquid filaments. These liquid filaments are then quenched in water to form a gel-fibre. The gel-fibre is drawn at a strain rate on the order of 1s^{-1} in hot air (at 120°C), resulting in a highly orientated and highly crystalline fibre of diameter $17\ \mu\text{m}$.
- II: Fibres are coated in a resin solution and are then formed into a $[0^\circ/90^\circ/0^\circ/90^\circ]$ stack. A drying process removes the matrix solvent from the stack, and several stacks are placed on top of each other in order to form the desired laminate.
- III: The laminate is hot pressed (the details are proprietary to DSM). Bonding of the layers is achieved through partial melting of the PU matrix material. The fibre diameter is unchanged by the hot-pressing operation, although a proportion of the fibres change their cross-sectional shape, as detailed in Russell et al. (2013).

An analogous process was used to manufacture the UD composites, and this is summarised as follows. Matrix-impregnated UD plies were laid-up into a plate of size $100\text{ mm} \times 100\text{ mm}$ and an areal density of 1.0 kgm^{-2} . These plies were then pressed together at a temperature of 127°C and a consolidation pressure of 20.6 MPa for 20 minutes to produce a UD laminate. All of the composite grades contain a fibre volume fraction of approximately 83%.

2.1. Grades of Dyneema[®] composites

The six grades differed in terms of the fibre and matrix type, ply thickness and stacking sequence: a summary of the grades, along with the designation

Designation	Commercial Designation	Fibre type	Matrix type	Ply thickness (μm)
SPC060	HB26	SK76	PADP	60
SSC060	HB50	SK76	SISTC	60
SPC120	N/A	SK76	PADP	120
SPC030	HB80	SK76	PADP	30
XSC060	N/A	Experimental	SISTC	60
SPU	N/A	SK76	PADP	N/A

Table 1: Summary of the six grades of the Dyneema[®] composites investigated in this study. The table specifies the fibre and matrix type and ply thickness along with the commercial designation (if any) and the designation employed here.

used to refer to them subsequently and the commercial designation (if any), is included in Table 1. The composite grades were made from four basic constituent materials: (i) two fibre types, SK76 and a stronger experimental fibre, and (ii) two types of polyurethane matrices, polyetherdiol-aliphatic diisocyanate polyurethane (PADP) and a weaker styrene-isoprene-styrene tri-block copolymer (SISTC), and then stacked with different ply thicknesses. The designations of the different grades are formulated as follows. The first letter corresponds to the fibre grade (S referring to SK76 and X to the experimental fibre), the second letter corresponds to the matrix type (with P and S corresponding to PADP and SISTC respectively), while the third letter gives the ply stacking sequence with C denoting the $[0^\circ/90^\circ]$ cross-ply stacking and U denoting the UD composite. The final three numbers in the designation give the ply thickness in microns; for the UD composite in which ply thickness is not relevant we omit these final three numbers. Thus, the designation SPC060 is a $[0^\circ/90^\circ]$ composite comprising SK76 fibres in a PADP matrix with 60 μm thick plies. This is the composite with the commercial designation HB26 while the composite with commercial designation HB50 is designated here as SSC060.

The differences between the grades is summarised as follows. SPC060 is taken to be the baseline material system while SPC030 and SPC120 have the same constituent materials (and hence similar tensile and shear properties) but different ply thicknesses. On the other hand, the SSC060 grade has the same ply thickness and fibre type as SPC060 but a matrix of SISTC with a lower shear yield strength. Similarly, the XSC060 grade uses the

experimental fibre which has a higher tensile strength, but the same matrix and similar ply thickness as the SSC060 system. Finally, the SPU grade is the UD composite with the same constituent materials as the reference SPC060 grade. Thus, these different grades enable an investigation of the effect of ply thickness, fibre strength and matrix strength as well as the stacking sequence. Measurements of the tensile and inter-laminar shear properties of the different grades are detailed in the following section to quantify the differences stated here.

Optical microscopy was used to examine the fibre/ply arrangements. Russell et al. (2013) have reported that bright field microscopy (and SEM observations) of the as-polished surface is misleading due to the presence of a very thin layer of smeared matrix and fibre material (of thickness on the order of a few microns). To obviate this problem, dark field microscopy was used to examine the stacking of the plies for all six grades of the Dyneema[®] composite; see Fig. 2. The dark field images give better contrast between fibre and matrix and reveals more clearly the cross-sectional shape of the fibre. The reference SPC060 laminate in Fig. 2(a) is comprised of orthogonally alternating plies, each with a thickness of approximately 60 μm .

2.2. Tensile and inter-laminar shear responses

Quasi-static material characterization tests were performed in order to measure properties that dictate the out-of-plane compressive responses of the composites. These were performed on all of the Dyneema[®] composites except the UD grade: the UD composite could not be gripped to perform valid material tests. Two types of tests were conducted:

- (i) Uniaxial tensile tests in an orientation such that the 0° plies were aligned with the tensile axis. The Dyneema[®] composites have a high tensile strength along the fibre directions, but a very low shear strength. Thus, a standard tabbed tensile specimen cannot be used as discussed by Russell et al. (2013). They employed a specimen with a large gripping area and a narrow gauge width as sketched in Fig. 3a. The tensile tests were conducted in a screw driven test machine at a nominal applied strain rate of 10^{-3}s^{-1} with the nominal stress determined by measuring the load from the load cell of the test machine. The axial nominal strain was measured using a clip gauge of gauge length 12.5 mm.
- (ii) Double-notch shear tests were used to measure the inter-laminar shear response, Fig. 3b. These tests were conducted using the double-notch

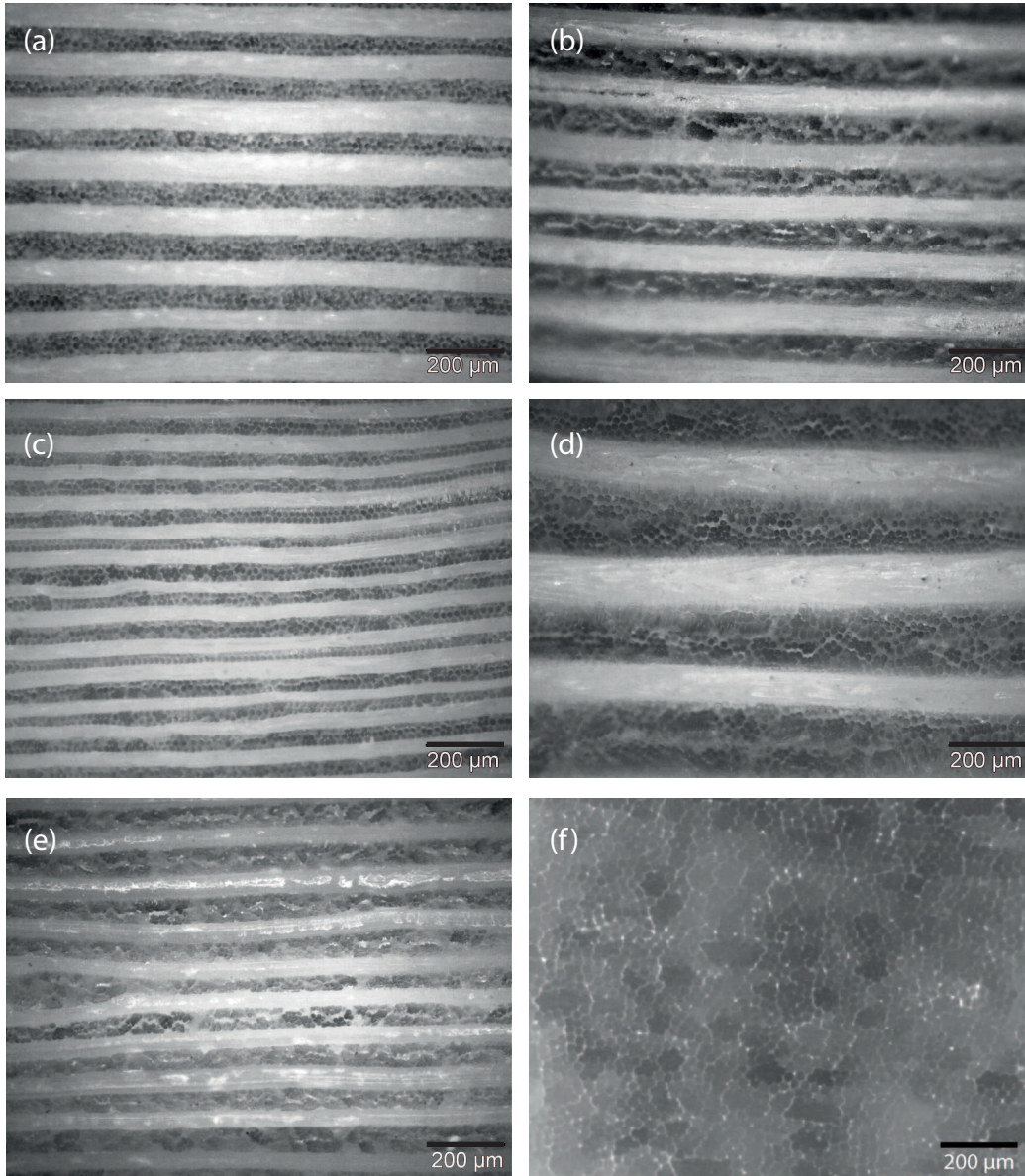


Figure 2: Dark field microscopy images of cross-sections of the different Dyneema[®] grades investigated in this study to show the ply arrangements: (a) SPC060, (b) SSC060, (c) SPC030, (d) SPC120, (e) XSC060 and (f) SPU.

specimen geometries (Liu et al., 2014) modified to suit the Dyneema[®] composites investigated in this study, as sketched in Fig. 3b. Specifically, strips of length 150 mm, width $b = 20$ mm and thickness 6 mm were cut from the Dyneema[®] composite sheets. Inter-laminar shear was promoted over a gauge length $c = 30$ mm by drilling one hole and 2 notches over the central section of the specimen as sketched in Fig. 3b. Care was taken to ensure that the hole/notches were positioned so that there were no continuous fibres that spanned the entire length of the specimen. The tests were conducted by friction gripping the specimen ends and pulling them, as indicated in Fig. 3b in a screw driven test machine. The inter-laminar shear stress τ_{31} was defined as $\tau_{31} \equiv P/(2cb)$, where P is the measured tensile load and the factor of 2 is present as the shear force P is shared by 2 inter-laminar planes, as shown by the dashed lines in Fig. 3b. The shear displacements were measured by mounting a clip gauge on either side of the notch. These tests were conducted at an applied displacement rate of 1 mm/min.

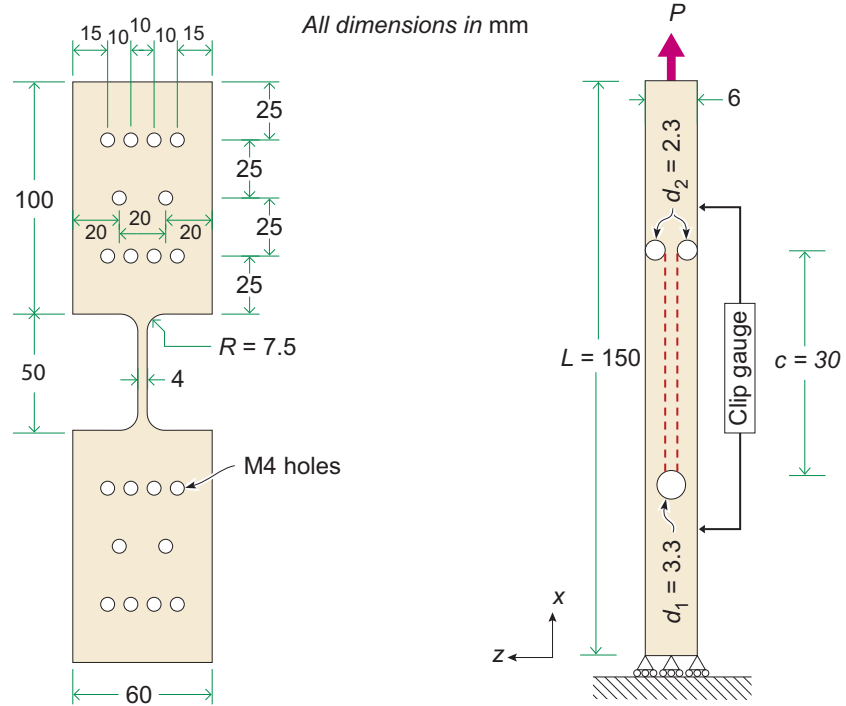
The tensile stress versus strain curves of the $[0^\circ/90^\circ]$ composites are plotted in Fig. 4a for an applied strain rate of 10^{-3}s^{-1} . All grades display an approximately elastic-brittle tensile response as the behaviour is mainly governed by the fibres. Hence, all the composites with SK76 fibres have a similar response with tensile strengths approximately equal to 800 MPa. On the other hand, the XSC060 grade with experimental fibres has a similar modulus to the other grades but a higher tensile strength of 880 MPa. The inter-laminar shear responses, as measured using the double-notch shear tests, are plotted in Fig. 4b. The peak shear strength of all the grades with the PADP matrix is around 1.5 MPa while the grades with the SISTC matrix is significantly lower at about 0.2 MPa. Similar to the observations reported in Liu et al. (2014), digital image correlation investigations of the deformation modes revealed that prior to peak load, deformation is reasonably homogeneous. However, at and after the peak stress, deformation strongly localises on two bands that emanate from the notches. This is consistent with the strongly softening nature of the inter-laminar shear response.

3. Out-of-plane compressive response

Consider Dyneema[®] specimens as sketched in Fig. 5a where X_i is the global co-ordinate system and x_i the local co-ordinate system of a single UD

(a) Tensile test specimen, top view

(b) Shear specimen, side view



Depth of specimen into the page = 6 mm Depth of specimen into the page, b = 20 mm

Figure 3: Sketches of the specimens employed to measure the (a) tensile response of the $[0^\circ/90^\circ]$ composites and (b) the inter-laminar shear response. Leading dimensions in mm are marked on the sketches.

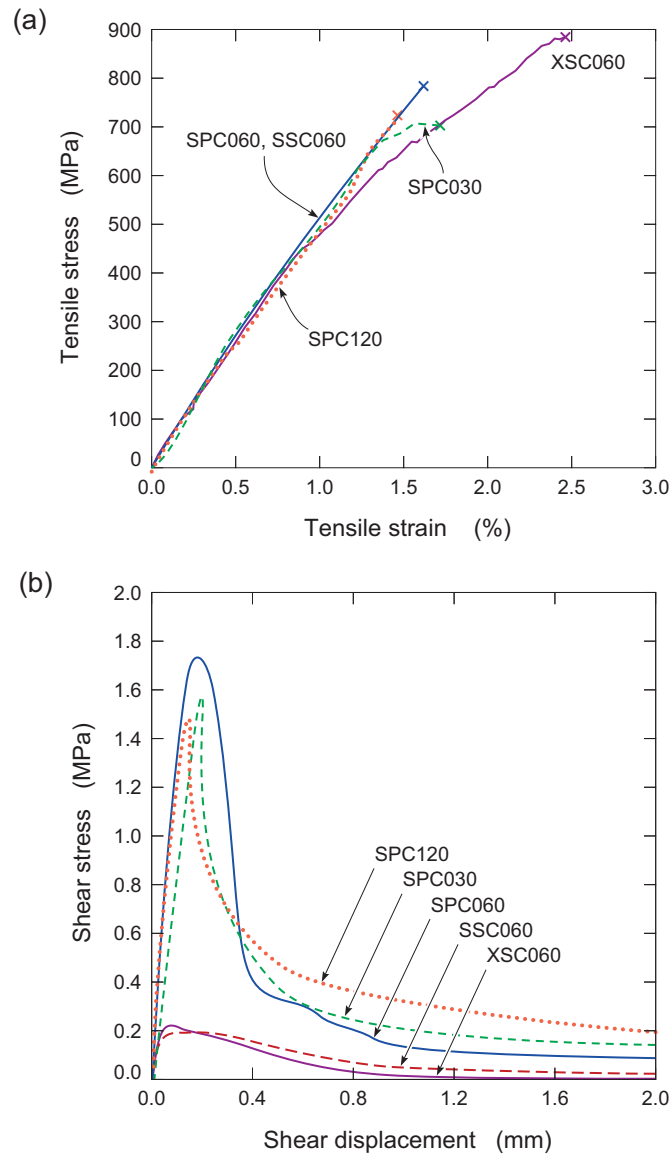


Figure 4: The measured (a) uniaxial tensile and (b) inter-laminar shear response for the $[0^\circ/90^\circ]$ composites.

ply as shown in the inset. We consider here the compressive response of these specimens in the X_3 direction. We anticipate the following response of a $[0^\circ/90^\circ]$ Dyneema[®] stack. Under through-thickness loading in the X_3 direction, each ply responds elastically along the fibre direction but can yield plastically in the transverse direction, as follows.

First, consider the case where the inter-ply shear strength is zero. Then, compression in the X_3 direction would activate yield within the plane normal to the local fibre direction, for each ply. Each ply would compress plastically in the X_3 direction and, assuming plastic incompressibility, would extend plastically in the direction transverse to the fibres (Fig. 5b). Consequently, the $[0^\circ/90^\circ]$ stack would deform by uniform plastic straining in the X_3 direction, along with in-plane extrusion transverse to the local fibre direction and negligible elastic straining along the fibre direction. Second, consider the practical case, where the inter-ply shear strength is finite. The unconstrained extrusion of each ply between its neighbours is now impeded by elastic axial deformation of neighbouring plies, and a shear lag zone exists near the side edge of each ply. The shear stress between each ply will lead to a progressive build-up of in-plane compressive stress within each shear lag zone of each ply transverse to the fibre direction.

The measurements and models described subsequently demonstrate that the out-of-plane compression of the $[0^\circ/90^\circ]$ Dyneema[®] composite results in a similar deformation mode, with each ply of the Dyneema[®] flowing only in the direction transverse to the fibre axis. For the case of in-plane specimen dimensions L much greater than the ply thickness h , we anticipate a significant build-up of pressure within each ply. These tests will be used to infer the pressure dependency of the shear strength of Dyneema[®] at pressures approaching the tensile strength of the Dyneema[®] composites (at pressures on the order of 1 GPa).

3.1. Experimental protocol

The out-of-plane compression tests (i.e. compression in the through thickness direction perpendicular to the plane of the plies as shown in Fig. 5b) were conducted on square Dyneema[®] specimens of in-plane dimensions L and thickness $t = 1$ mm. These specimens were cut from 1 mm thick Dyneema[®] sheets with a sharp razor blade. No delamination was visible on the edges of the samples and vernier callipers were used to measure the side lengths and thickness of each sample before testing. The specimens were compressed

between hardened silver steel platens (hardness 6.87-7.26 GPa) in a screw-driven test machine at a compression rate of 0.2 mm/min. The applied load was measured from the load cell of the test machine and used to infer the applied nominal stress. A clip gauge attached across the platens was used to measure the compressive displacement from which the nominal compressive strain applied to the specimen was calculated. The compression of each specimen was photographed via a Nikon D7000 DSLR camera with a digital resolution of 300dpi and an image size of 3696 x 2448 pixels. For each sample size and grade, approximately 10 tests were performed- the large number of tests were required to obtain an average that was not unduly influenced by dimensional tolerance, damage to the sample pre-testing or defects within the specimens.

3.2. Summary of measurements and results

We first summarise results for the reference SPC060 Dyneema[®] grade. The measured applied nominal compressive stress σ_n versus compressive nominal strain ε_n curves for selected square specimens with lateral size L in the range 3 to 10 mm are included in Fig. 6. The curves are divided into two groups: Fig. 6a shows the response of specimens with sizes $L \leq 4$ mm, while specimens of sizes $L > 4$ mm are shown in Fig. 6b. The two groups display remarkably different responses.

First consider the small specimen sizes. The compressive nominal stress versus strain responses initially exhibit linear elastic behaviour followed by a regime where the applied nominal stress increases negligibly with increasing compressive strain (referred to subsequently as the plateau regime). There is a steep rise in the nominal stress beyond $\varepsilon_n = 0.4$. Some representative unloading curves are also included in Fig. 6a, illustrating the significant permanent deformation seen upon unloading in the plateau regime. This suggests that the specimens are deforming plastically after the initial elastic response. We conclude that the material deforms in a plastic manner with lateral (Poisson) expansion resulting from the near incompressible nature of the deformation. The sharp rise in the nominal stress beyond $\varepsilon_n = 0.4$ is due to an increase in the cross-sectional area of the specimen and is exacerbated by friction between the specimen and the loading platens.

Next, consider the response of the larger specimens in Fig. 6b. In contrast to the smaller specimens, these samples display an approximately linear elastic response (as evidenced from the selected unloading curves included for the $L = 10$ mm specimen) with the stress rising to the 300-900 MPa range.

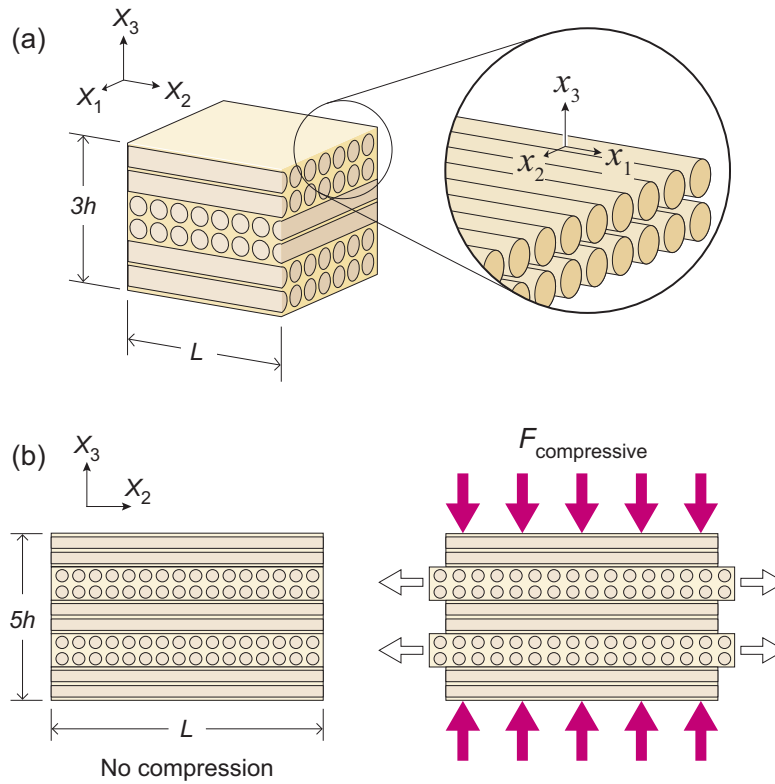


Figure 5: (a) Sketch of a $[0^\circ/90^\circ]$ composite specimen of side L and thickness $3h$ subjected to out-of-plane compression. The global co-ordinate system X_i is indicated. The inset shows a single UD ply along with the associated local co-ordinate system x_i such that the fibres lie along the x_1 and the ply lies in the $x_1 - x_2$ plane. (b) Sketch showing the deformation mode with plies extruding out transverse to the fibre direction.

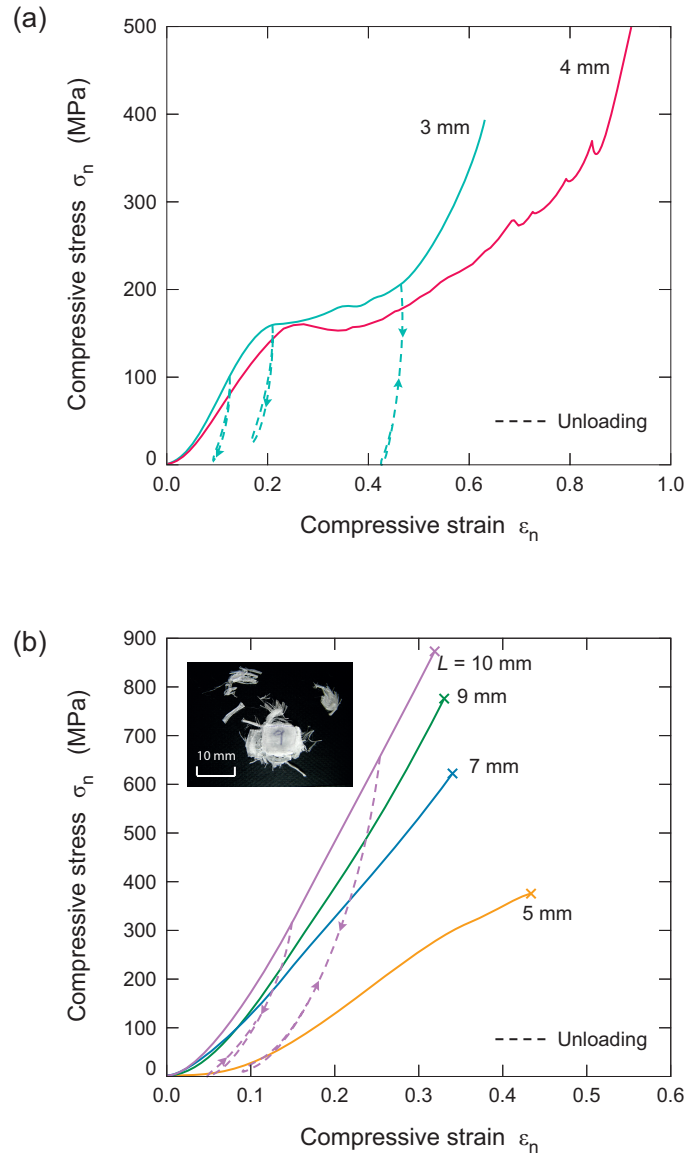


Figure 6: The measured compressive stress σ_n versus strain ϵ_n responses of the SPC060 Dyneema[®] composites for specimen size (a) $L \leq 4$ mm and (b) $L > 4$ mm. The inset in (b) shows an image of a failed $L = 9$ mm specimen.

At the peak stress σ_{\max} , catastrophic failure occurs, resulting from failure of the fibres and accompanied by significant acoustic emission: the top view of the remnants of the $L = 9$ mm specimen after failure are shown in the inset of Fig. 6b. The deformation mode is shown in Fig. 7a as a montage of photographs of the progressive deformation of a $L = 6$ mm specimen. It is clear that prior to catastrophic failure of the specimen there is no lateral expansion, but rather alternate plies are seen to be extruded outwards. Upon a closer examination, the deformation mode was that sketched in Fig. 5b where alternate 0° and 90° plies extruded out of the free surfaces of the specimen perpendicular to the fibre directions. An image of the specimen after catastrophic failure has occurred is shown in Fig. 7b. The extruded plies contained only fibres oriented transversely to the extrusion direction.

In order to better understand the deformation mechanisms leading to tensile fibre fracture under compressive loading we performed an X-ray computed tomography (CT) scan¹ on a $L = 8$ mm specimen. MicroXCT images of the $X_2 = 0$ plane were taken to reveal the deformation near the free surface of the specimens as shown in the inset in Fig. 8. Two images are shown in Fig. 8: in (a) a pair of scans are digitally stitched to show the undeformed specimen, while (b) shows two scans of the same specimen after loading to a nominal compressive stress of 600 MPa and then unloaded. Voids in the specimen are shaded in blue: while initially there is a near uniform distribution of voids in the specimen as seen in Fig. 8a, it is clear from Fig. 8b that loading to 600 MPa has resulted in a gradient in the void density being developed such that there is a higher void density near the free surface. We associate these voids with deformation in or damage to the specimen. These micrographs indicate that deformation is primarily occurring near the free surfaces of the specimen.

In order to illustrate the effect of the regime of intense deformation around the periphery of the specimen we performed compression tests on a $L = 25$ mm specimen with pressure sensitive films² placed between the specimen and the loading platen. The film contains a layer of microcapsules filled with red ink. This ink is released at a rate dependent on the local pressure, such that the intensity of the colour is proportional to the observed pressure.

¹Xradia (Concord, CA) MicroXCT-200 tomographic imaging system. Resolution was $1.3646 \mu\text{m}/\text{voxel}$ with source anode settings 35 kV and 7W.

²Fujifilm Prescale (Fujifilm Corp., Japan). The HS grade (50-130 MPa) and HHS grade (130-300 MPa) were used in conjunction.

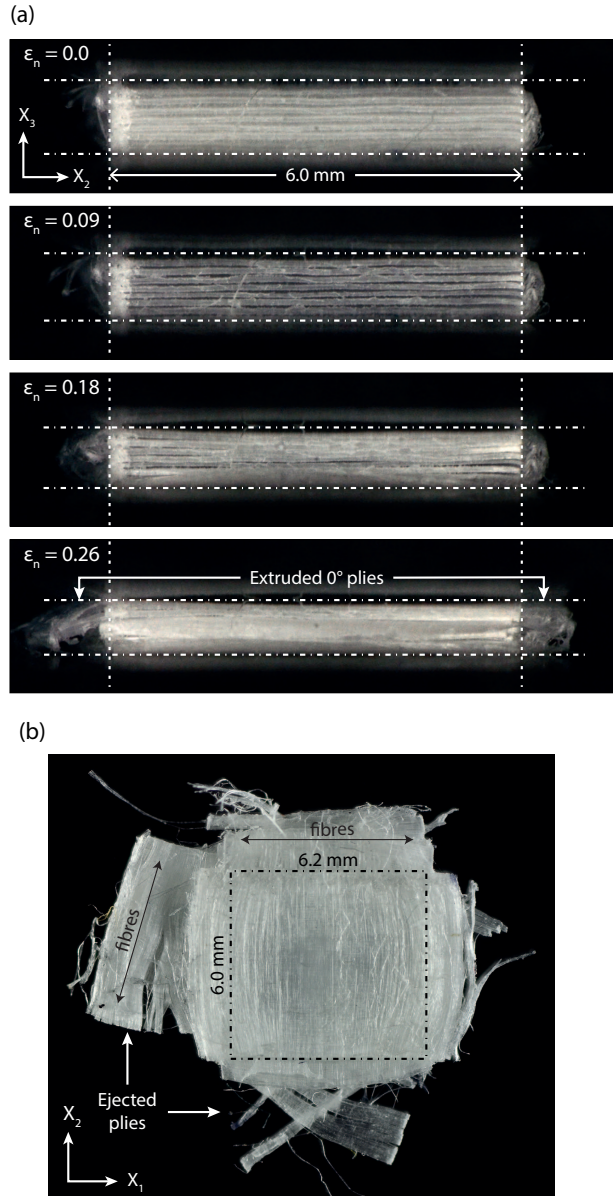


Figure 7: (a) Montage of images showing the deformation of the $L = 6$ mm SPC060 specimens undergoing out-of-plane compression. The global co-ordinate system is indicated and values of ε_n for the images are marked. (b) A top view image of the same specimen after failure, showing the ejected plies.

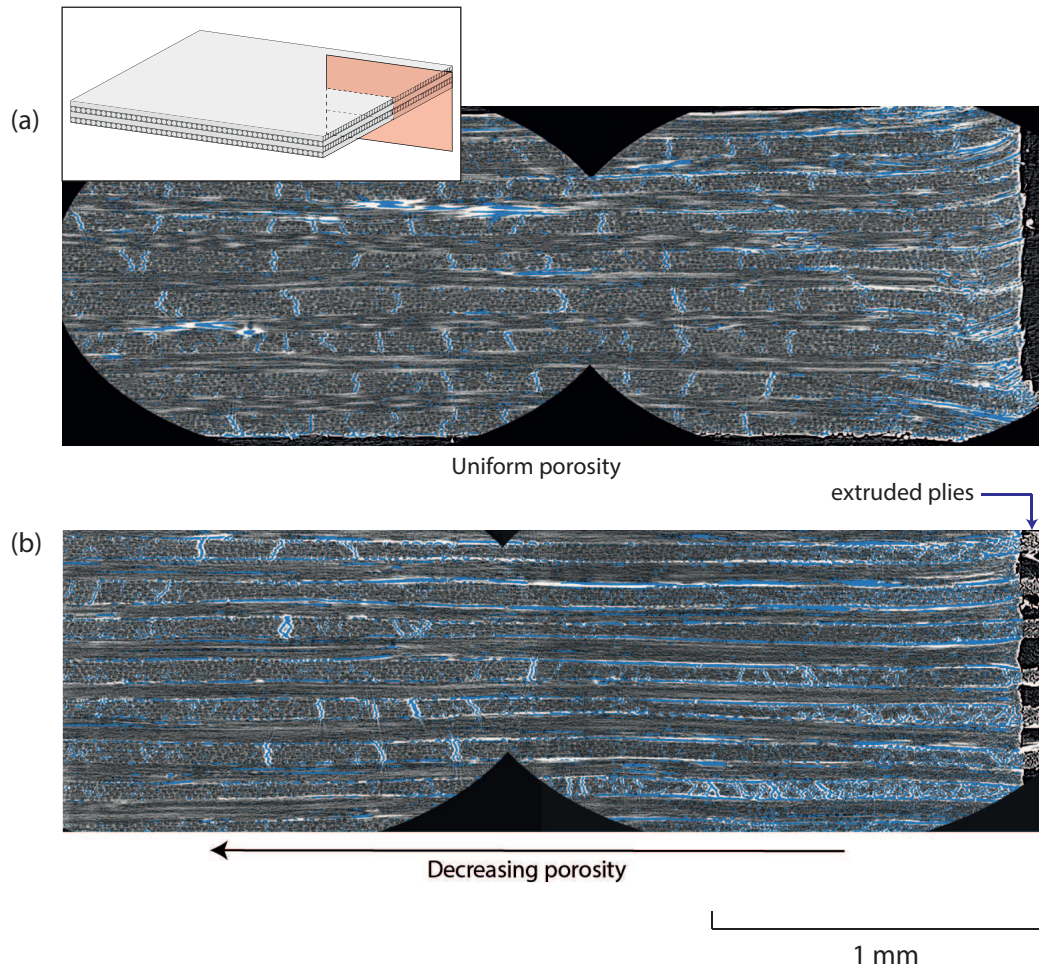


Figure 8: X-ray scans showing the $X_2 = 0$ plane of $L = 8$ mm SPC060 specimen (a) prior to loading and (b) loaded to a stress $\sigma_n = 600$ MPa and then unloaded. The voids in the specimen are shaded in blue and the inset shows a sketch of the region of the specimen included in the images.

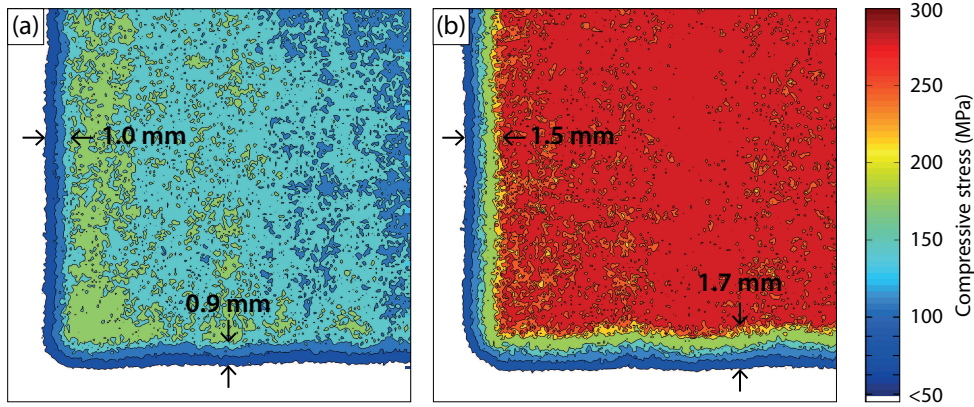


Figure 9: Contour plots of the pressure between the $L = 25$ mm SPC060 specimen and the loading platen after application of a stress (a) $\sigma_n = 100$ MPa and (b) $\sigma_n = 200$ MPa. Only a 15 mm corner section of the specimen is shown for the sake of clarity.

Layers of the HS and HHS grades of pressure sensitive film were stacked on top of the specimen to ensure that the full range of test pressures could be recorded. The films were scanned³ at each unloading point to produce a digital image of the loading. The pixel intensity values were measured and used to create a pressure map. Contour plots of the stresses recorded by the film after loading the specimen to nominal stress levels of $\sigma_n = 100$ MPa and 200 MPa are included in Figs. 9a and 9b, respectively. It is clear that the pressure over the specimen is approximately constant over a central patch and then diminishes towards the specimen edges. This region of pressure decrease approximately corresponds to the region of intense deformations seen in Fig. 8b. This insight shall be used to develop a shear lag model for the compressive deformation of the Dyneema[®] specimens in Section 5.

A summary of the peak strength σ_{\max} measurements of the reference SPC060 Dyneema[®] grade are included in Fig. 10 as a function of the specimen length L . (A discussion of the scatter in the measured values of σ_{\max} for the SPC060 and SSC060 composites is presented in the Appendix). Only data from specimens which displayed a distinct peak strength is included in Fig. 10, i.e. as discussed above, fibre failure is not observed for specimens with $L < 4$ mm. These specimens did not display a peak strength and hence

³Epson Perfection V500 Photo Scanner at a resolution of 2400 dpi

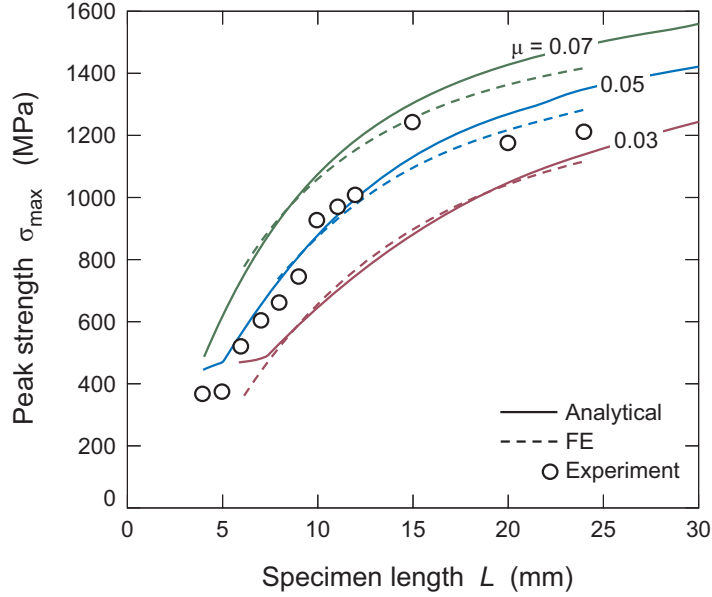


Figure 10: Measurements and predictions of the peak strength σ_{\max} of the SPC060 Dyneema[®] specimens as a function of the specimen size L . Both FE and analytical predictions are included for three selected values of the pressure sensitivity co-efficient μ .

that data is excluded from Fig. 10. For specimens with $L > 4$ mm, the peak nominal strength increases with increasing L and then begins to plateau at a value of approximately 1200 MPa for $L > 15$ mm. This size dependency of the compressive strength will be explained in Section 5 via a shear lag analysis. We proceed to examine the dependence of this size effect on lay-up and material parameters.

3.2.1. Effect of stacking sequence

The measured compressive nominal stress σ_n versus nominal strain ε_n curves for the SPU Dyneema[®] grade (i.e. UD composite) are shown in Fig. 11a for selected specimen sizes in the range $9 \text{ mm} \leq L \leq 13 \text{ mm}$. The responses over the the entire range of specimen sizes tested are rather similar to the SPC060 Dyneema[®] grade response for specimen sizes $L < 4$ mm, i.e. the nominal stress increases rather gradually up to a nominal strain $\varepsilon_n = 0.4$ after which it rises steeply. In addition, no catastrophic failure of the specimen was observed even after compression to nominal strains of about 80%. Selected unloading curves of the $L = 13$ mm specimen are

included in Fig. 11a and clearly show that forward loading generates a plastic response, while unloading results in negligible strain recovery. A montage of photographs of the side of a sample, showing the progressive deformation of the $L = 13$ mm SPU specimen, is included in Fig. 11b. We observe that the specimens deform in a plastic manner with shear band formation and significant lateral expansion, similar to the behaviour of the small specimens, as shown in Fig. 6a.

It is instructive to compare the strengths of the SPU and SPC060 composites as the only difference between these two grades is the lay-up of the plies, with the matrix and fibres identical in the two cases. No catastrophic failure was observed in the SPU composites, and thus to make a fair comparison we plot in Fig. 12 the measured nominal stress of the SPU composite specimens at an applied nominal strain of 40% (recall that the SPC060 specimens all failed at compressive strains of around 40%; see Fig. 6b). There are two stark differences between the SPU and SPC060 specimens: (i) the strength of SPU specimens shows no discernable size effect for specimen lengths $L \leq 24$ mm while a clear size dependence is seen in the SPC060 specimens and (ii) the peak strength of the SPC060 specimens range from about 300 MPa to about 1200 MPa while the SPU specimens have a strength of about 20 MPa. We deduce that the interaction between the 0° and 90° plies causes the significant strength enhancement of the SPC060 composites, and the precise mechanism will be clarified in Section 5.

3.2.2. *Effect of ply thickness*

The SPC030 and SPC120 grades are identical to the SPC060 grade in every respect other than ply thickness (the matrix and fibres are identical for these three grades). The measured compressive responses of the SPC030 and SPC120 composites are qualitatively similar to the SPC060 composites, and the peak strengths are compared in Fig. 12. In all cases, the peak strength increases with L and the strength asymptotes to a constant value at large specimen sizes. Moreover, it is clear that, over the range of specimen sizes investigated here, the peak strength increases with decreasing ply thickness even though the tensile and inter-laminar shear responses are insensitive to ply thickness; see Fig. 4.

3.2.3. *Effect of matrix shear strength*

The SSC060 grade has the same ply lay-up, ply thickness and fibre type as the SPC060 grade but contains a matrix of lower shear strength as is

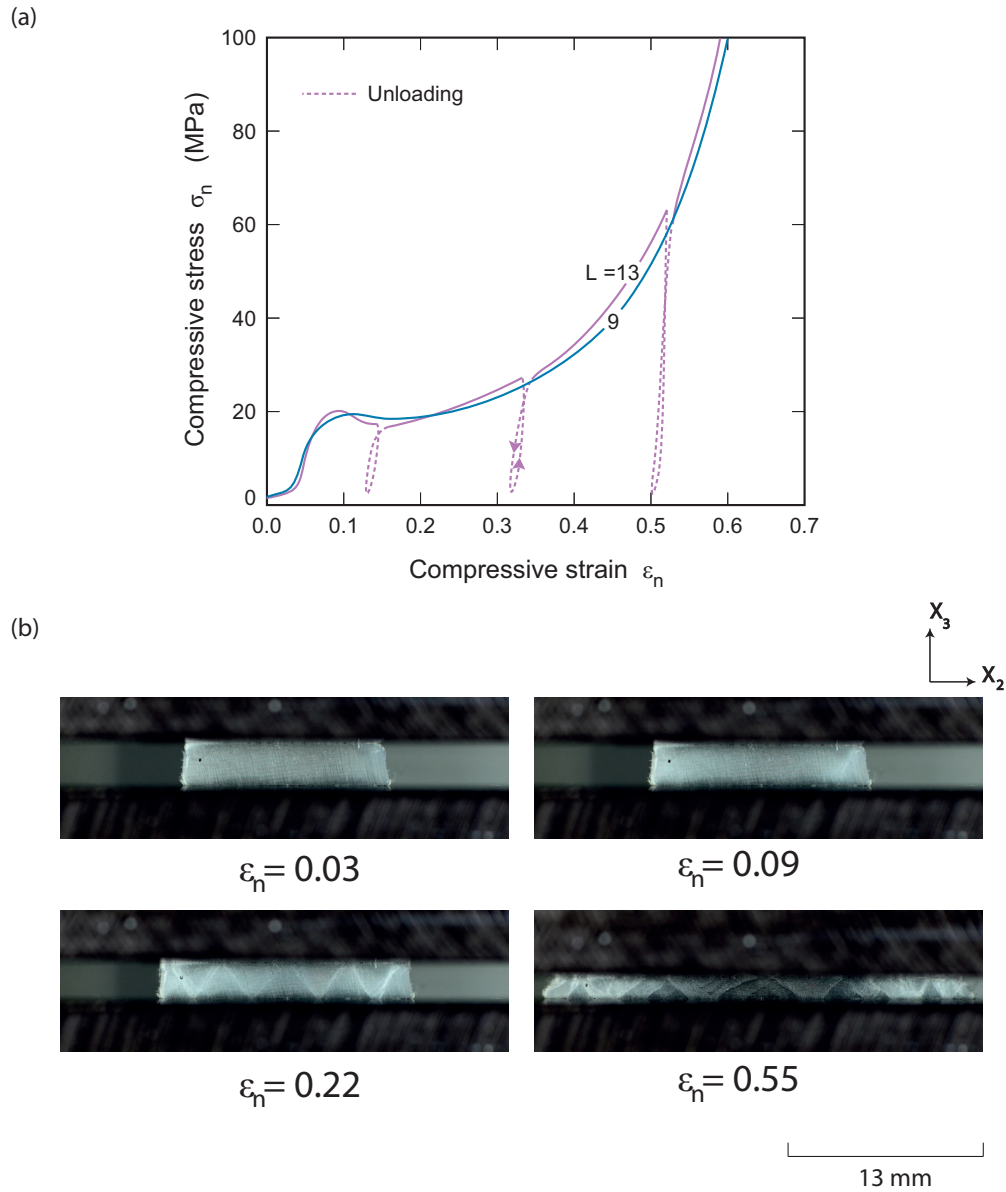


Figure 11: (a) The measured nominal stress σ_n versus nominal strain ε_n curves of the SPU Dyneema[®] for specimens sizes in the range $9 \text{ mm} \leq L \leq 13 \text{ mm}$. (b) Montage of images showing the deformation of the $L = 13 \text{ mm}$ SPU specimen. The global co-ordinate system is indicated and the values of ε_n for the images are marked.

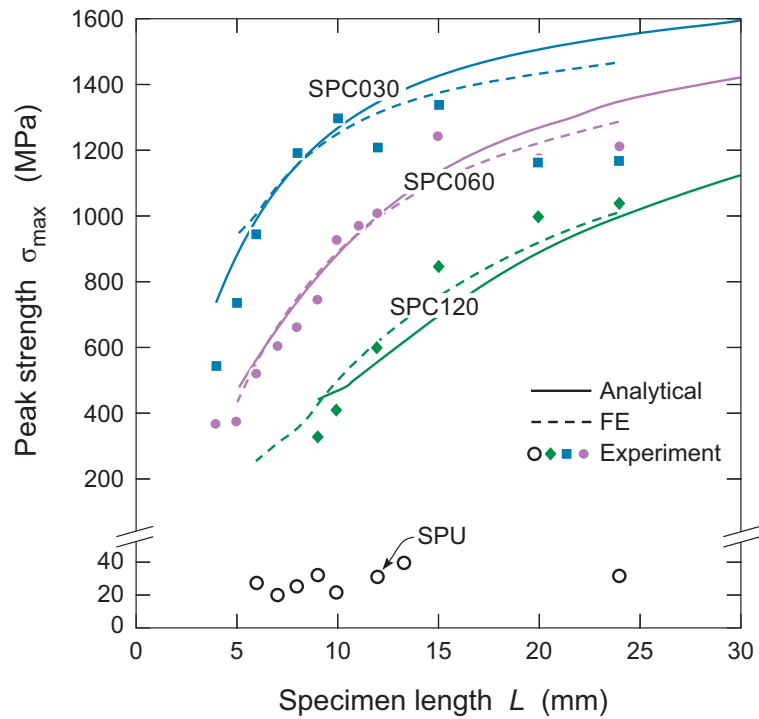


Figure 12: The measured peak strengths σ_{\max} as a function of specimen size L of composites with SK76 fibres and PADP matrix to show the effect of ply thickness and stacking sequence. Measurements for grades SPC030, SPC060, SPC120 and SPU are included along with the corresponding FE and analytical predictions for the $[0^\circ/90^\circ]$ composites.

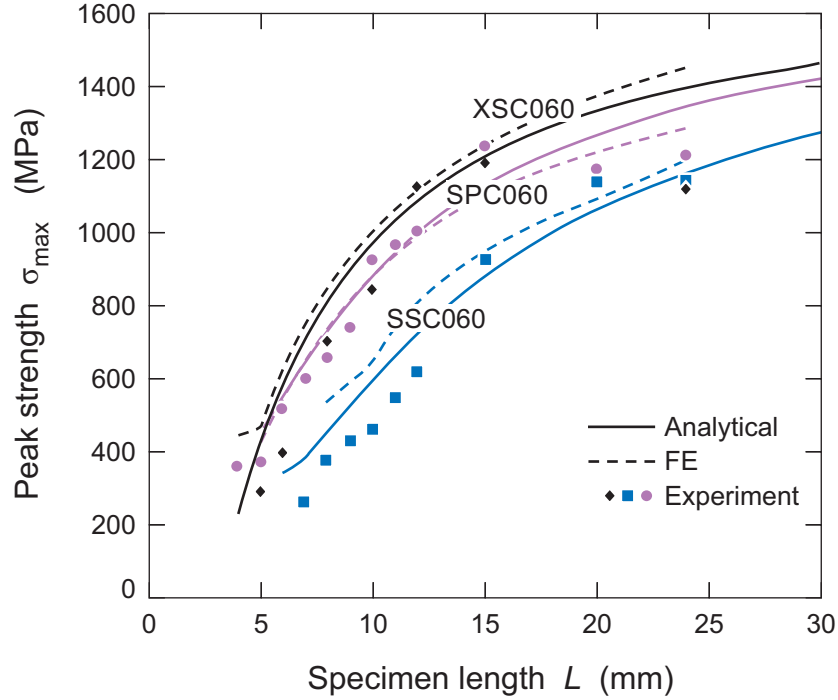


Figure 13: The measured peak strengths σ_{\max} as a function of specimen size L of the SPC060, SSC060 and XSC060 composites to show the effect of fibre and matrix strength. The corresponding FE and analytical predictions are also included.

evident from the inter-laminar shear strengths of the SPC060 and SSC060 grades in Fig. 4. Thus, the effect of the matrix shear strength on the compressive response can be obtained. The compressive responses of the SPC060 and SSC060 grades are qualitatively similar as shown in Fig. 13. The peak strength variation with L of the SSC060 grade is similar to that of the SPC060, albeit the SSC060 has a lower strength over the range of specimen sizes tested here. We attribute this difference to the lower shear strength of SSC060 compared to SPC060.

3.2.4. Effect of fibre strength

Finally, we note that the XSC060 grade is identical to the SSC060 grade in every respect other than fibre strength. The experimental fibres have a higher strength and this results in a higher tensile strength of the composite: compare the inter-laminar shear and tensile strengths of the XSC060 and SSC060 grades in Fig. 4. The peak strengths of the XSC060 are higher

compared to the SSC060 grade, but qualitatively similar, over the range of specimen sizes tested here, see Fig. 13. We attribute this increase in the compressive strength of the XSC060 grade to the higher fibre strength in these composites.

4. Finite element model for the out-of-plane compressive response of Dyneema[®] composites

We proceed to model the compressive response of the Dyneema[®] composites. First, a constitutive model for Dyneema[®] is proposed and the out-of-plane compressive response is predicted via Finite Element (FE) calculations. These FE calculations are then used to motivate an analytical model which yields simple closed-form expressions for the out-of-plane compressive stress versus strain response and the peak strength of $[0^\circ/90^\circ]$ Dyneema[®] composites.

4.1. Constitutive model for a single ply

An elastic-ideally plastic constitutive model for a single UD ply of Dyneema[®], as sketched in the inset of Fig. 5a, is proposed in this section. The ply lies in the $x_1 - x_2$ plane with the fibre axis in the x_1 direction; x_3 is the out-of-plane direction. The total strain rate $\dot{\epsilon}_{ij}$ is written as the sum of an elastic $\dot{\epsilon}_{ij}^e$ and plastic components $\dot{\epsilon}_{ij}^p$:

$$\dot{\epsilon}_{ij} = \dot{\epsilon}_{ij}^e + \dot{\epsilon}_{ij}^p. \quad (2)$$

For an elastic, transversely isotropic ply with the x_1 fibre direction normal to the plane of isotropy, the elastic strain rate is written in terms of the stress rate $\dot{\sigma}_{ij}$ as:

$$\begin{pmatrix} \dot{\epsilon}_{11}^e \\ \dot{\epsilon}_{22}^e \\ \dot{\epsilon}_{33}^e \\ \dot{\epsilon}_{23}^e \\ \dot{\epsilon}_{13}^e \\ \dot{\epsilon}_{12}^e \end{pmatrix} = \begin{pmatrix} 1/E_f & -\nu_{12}/E_f & -\nu_{12}/E_f & 0 & 0 & 0 \\ -\nu_{12}/E_f & 1/E_m & -\nu_{23}/E_m & 0 & 0 & 0 \\ -\nu_{12}/E_f & -\nu_{23}/E_m & 1/E_m & 0 & 0 & 0 \\ 0 & 0 & 0 & (1+\nu_{23})/E_m & 0 & 0 \\ 0 & 0 & 0 & 0 & 1/(2G_{12}) & 0 \\ 0 & 0 & 0 & 0 & 0 & 1/(2G_{12}) \end{pmatrix} \begin{pmatrix} \dot{\sigma}_{11} \\ \dot{\sigma}_{22} \\ \dot{\sigma}_{33} \\ \dot{\sigma}_{23} \\ \dot{\sigma}_{13} \\ \dot{\sigma}_{12} \end{pmatrix}, \quad (3)$$

where E_f and E_m are the ply Young's moduli in the fibre direction x_1 and transverse direction x_2 , respectively, while ν_{21} and ν_{23} are the Poisson's ratios in the $x_1 - x_2$ and $x_2 - x_3$ plane, respectively. The shear modulus in the $x_1 - x_2$ plane is denoted as G_{12} . Now consider the plastic response. To retain consistency with the anisotropic elastic response, we propose an anisotropic yield criterion based on the following considerations:

- (i) The ply is treated as elastic in the fibre direction.
- (ii) In all other directions, ply yielding is assumed when the maximum shear stress reaches a shear yield strength similar to the Tresca criterion for metals.
- (iii) However, unlike metal plasticity, the shear yield strength of polymers (including PE) is pressure dependent; see for example Ward (1971). We include a pressure dependency in the yield function, and substantiate this assertion by comparing measurements and predictions in the following sections.
- (iv) We propose that plastic straining is incompressible, i.e. the flow rule is non-associated; see Ward (1971) for substantiation of this assumption.
- (v) Although Dyneema[®] is mildly rate sensitive (Russell et al., 2013; Karthikeyan et al., 2013a), the rate sensitivity is not explored within this investigation and all measurements are performed at a fixed strain rate of 0.1 s^{-1} . Thus, for the purposes of this study it suffices to model the Dyneema[®] as a rate-independent plastic solid.

Based on the above assumptions we propose a yield surface F comprising of four facets

$$f_1 \equiv \frac{|\sigma_{22} - \sigma_{33}|}{2} - \mu p \quad (4a)$$

$$f_2 \equiv |\sigma_{12}| - \mu p \quad (4b)$$

$$f_3 \equiv |\sigma_{23}| - \mu p \quad (4c)$$

$$f_4 \equiv |\sigma_{13}| - \mu p, \quad (4d)$$

where $p \equiv -(\sigma_{22} + \sigma_{33})/2$ is the in-plane pressure in the $x_2 - x_3$ plane and the friction parameter μ is non-negative, and quantifies the pressure sensitivity of the yield surface. Yielding occurs when the yield criterion is attained:

$$F \equiv \max(f_1, f_2, f_3, f_4) - \tau_0 = 0. \quad (5)$$

Here τ_0 is the shear yield strength of Dyneema[®] at zero pressure, $p = 0$. It remains to specify the incompressible plastic flow rule. Corresponding to each yield facet f_k we define a flow potential g_k given by

$$g_1 \equiv \frac{|\sigma_{22} - \sigma_{33}|}{2} \quad (6a)$$

$$g_2 \equiv |\sigma_{12}| \quad (6b)$$

$$g_3 \equiv |\sigma_{23}| \quad (6c)$$

$$g_4 \equiv |\sigma_{13}|, \quad (6d)$$

such that g_1 is the flow potential corresponding to the yield condition f_1 and so on. Assuming plastic flow with no hardening, the plastic strain rate is written as

$$\dot{\epsilon}_{ij}^p = \dot{\lambda}_k \frac{\partial g_k}{\partial \sigma_{ij}}, \quad (7)$$

where $\dot{\lambda}_k$ is the non-negative plastic multiplier associated with each flow potential (and the usual summation convention applied for a repeated suffix). Note that in cases where two or more yield facets f_k are active, i.e the stress state is at a corner of the yield surface, the plastic strain rate is the sum over two or more flow potentials as given by the sum over the subscript k in Eq. (7); see Koiter (1953) for a detailed discussion on plastic flow for materials with a singular yield surface.

4.2. Reference material parameters

The constitutive model proposed above requires the specification of five elastic constants and two plastic parameters τ_0 and μ . The values for each of the Dyneema[®] composites listed in Table 2 are compiled using data from Russell et al. (2013), Liu et al. (2014) and the measurements as detailed in Section 2.2. The Poisson ratios have not been measured, but are deduced from the following arguments: (i) transverse compression of the fibres is not expected to result in straining along the fibre direction and hence we set $\nu_{21} = 0$, and (ii) compression in the x_3 direction is expected to result in near incompressible deformation of the ply and hence we take $\nu_{23} = \nu = 0.5$. We shall show subsequently that the appropriate value for the pressure sensitivity coefficient is $\mu = 0.05$ for all grades, except for XSC060, for which $\mu = 0.07$.

4.3. Compressive response predictions

We proceed to present FE simulations of the out-of-plane compressive response of the SPC060 grade composite specimen. The simulations were performed using the explicit version of the commercial finite element package ABAQUS with the constitutive model described above implemented as a user material subroutine (VUMAT). For computational efficiency we model a specimen comprising an infinite number of alternate 0° and 90° plies as follows. Consider a square specimen of side L in the $X_1 - X_2$ plane with the X_3 direction corresponding to the out-of-plane compression direction. As the specimen comprises an infinite number of alternate 0° and 90° plies each of thickness h , it suffices to only model two adjacent 0° and 90° plies with the

origin of the co-ordinate system fixed at the geometric centre of this two ply specimen. We then enforce periodic boundary conditions on the top and bottom surfaces, i.e. on $X_3 = \pm h$. To define these periodic boundary conditions consider locations A and B on the top and bottom surfaces, respectively, with identical X_1 and X_2 co-ordinates. The displacements at these locations are constrained as follows

$$u_1^{(A)} - u_1^{(B)} = 0 \quad (8a)$$

$$u_2^{(A)} - u_2^{(B)} = 0 \quad (8b)$$

$$u_3^{(A)} - u_3^{(B)} = -2h\varepsilon_n, \quad (8c)$$

where the superscripts (A) and (B) refer to the two locations, and ε_n is the imposed compressive nominal strain. The symmetry of the problem implies that we need only analyse a quarter of the specimen. This is achieved by imposing symmetry boundary conditions corresponding to $u_1 = 0$ along $X_1 = 0$ and $u_2 = 0$ along $X_2 = 0$. Displacement continuity is assumed along the interface between the two plies.

The SPC060 grade was modelled using the reference material properties detailed above, with the ply thickness taken to be $h = 60 \mu\text{m}$, consistent with the observations in Fig. 2a. As the simulations are performed using an explicit FE scheme we need to specify the material density. This was assumed to be $\rho = 970 \text{ kgm}^{-3}$, in accordance with the manufacturer's data. To ensure that the simulations are representative of quasi-static loading, a small loading rate $\dot{\varepsilon}_n$ was used such that inertial effects remain negligible (the kinetic energy is small compared to the total energy). The specimen was discretised using eight-noded linear brick elements with reduced integration (C3D8R in the ABAQUS notation). Simulations are reported for two mesh sizes with cuboidal elements of length $h/7$ and $h/12$ (in the thickness direction) in order to investigate the sensitivity of the predictions to the element size.

Predictions of the applied compressive nominal stress σ_n (calculated as the work conjugate to the applied strain ε_n) versus the compressive nominal strain ε_n are plotted in Fig. 14a for the $L = 7 \text{ mm}$ and $L = 10 \text{ mm}$ SPC060 specimens for both element sizes considered here. The FE calculations predict an initial linear elastic response followed by deviation from linearity for $\varepsilon_n > 0.05$. The simulations are truncated at $\varepsilon_n = 0.18$ but it is worth mentioning here that no material failure is included in the model and hence these simulations do not directly predict a peak strength as observed in the exper-

iments⁴. The mesh dependence arises because the coarse mesh is not able to capture the stress distribution in the shear lag region. The predictions of the distribution of plastic strain ϵ_{23}^p within the plies is shown in Figs. 14b and 14c for the two mesh sizes considered here. In these figures, contours of the plastic strain ϵ_{23}^p on the $X_1 = 0$ plane are plotted on the undeformed meshes at an applied $\epsilon_n = 0.1$ (the fibre orientations on this section are also sketched in the inset of the figure). It is clear that the shear strain localises within one element of the interface between the plies, i.e the predicted plastic strain distribution is mesh dependent for the cases shown here. In fact, further mesh refinements revealed increasing localisation of plastic straining at the interface between the plies, suggesting that the converged solution is a slip discontinuity between the plies that is not accurately captured in this approach.

4.4. Model with slip on interface

The FE simulations of Section 4.3 show localisation of plastic shear strain at the interface between the plies with negligible shearing in the remainder of the ply. This suggests that a numerically more efficient model for the the Dyneema[®] composite would be to exclude plastic shear straining within the ply, and simply include this as an interface slip condition between the plies. Motivated by this insight, we propose a modification to the constitutive description used above to model the compression of Dyneema[®]. Subsequently, we shall refer to the model of Section 4.3 as the *full model*, and the modification presented here as the *reduced model*.

The details of the reduced model are as follows. Each UD Dyneema[®] ply of thickness h is split into three layers: two interface layers of thickness h_i and a layer that models the bulk of the ply (referred to subsequently as the core layer) sandwiched between these two interface layers as sketched in Fig. 15a. The thickness of the interface layers $h_i \ll h$ is such that the thickness h_i does not significantly affect the results, however, its presence is required for the numerical implementation of the model as will be made clear subsequently. We proceed to specify the constitutive description for the interface and core layers respectively. The notation used is identical to Section 4.1 with the x_1 direction referring to the fibre direction.

⁴Predictions of the peak strength may be deduced from these calculations as a post-processing step and this will be discussed subsequently in Section 4.6.

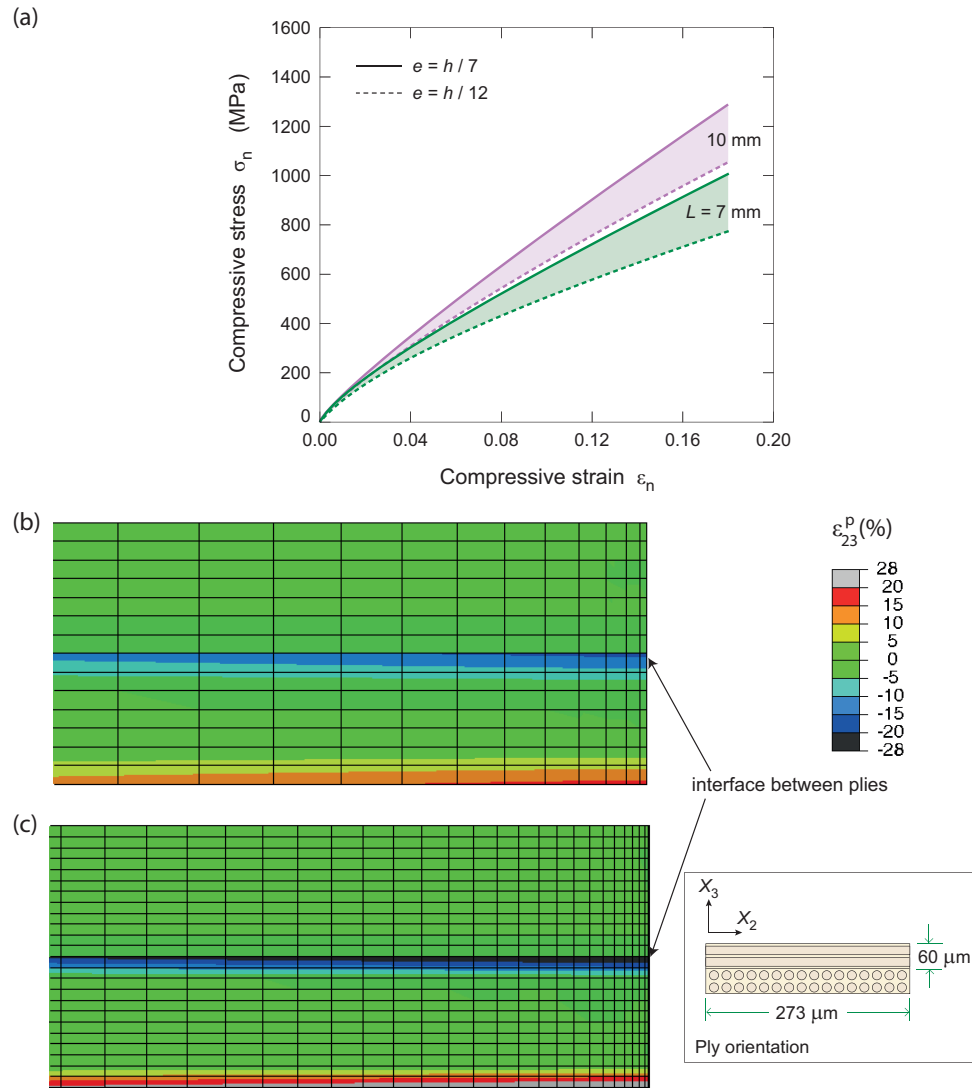


Figure 14: (a) FE predictions of the σ_n versus ε_n response of the SPC060 grade for selected values of specimen size L and two mesh sizes e . FE predictions of the distribution of the plastic strain ε_{23}^p on the $X_1 = 0$ plane for a mesh size (b) $e = h/7$ and (c) $e = h/12$. The fibre orientation in each ply for (b) and (c) is sketched in the inset.

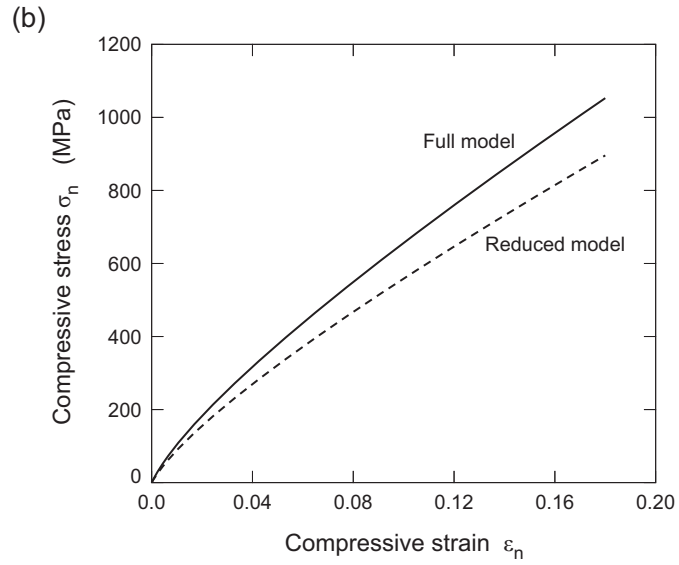
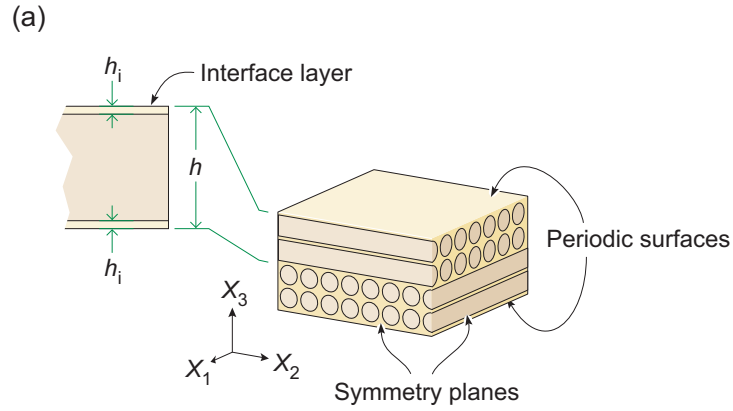


Figure 15: (a) Sketch illustrating the reduced FE model wherein each ply of thickness h is split into 3 layers: a core layer sandwiched between two interface layers thickness h_i . (b) Comparison between the FE predictions of the σ_n versus ϵ_n response of the $L = 10$ mm SPC060 composite using the full ($e = h/12$) and reduced FE models.

The model for the core is identical to that in Section 4.1 with one exception. The plastic yield surface is $F = \max(f_1, f_2)$ and the corresponding flow rule is also then modified to only include two yield facets, i.e.

$$\dot{\varepsilon}_{ij}^p = \dot{\lambda}_1 \frac{\partial g_1}{\partial \sigma_{ij}} + \dot{\lambda}_2 \frac{\partial g_2}{\partial \sigma_{ij}}. \quad (9)$$

Thus, out-of-plane shear yielding within the core is excluded but plastic yielding due to direct stresses in the $x_2 - x_3$ plane, and shearing in the $x_1 - x_2$ plane are permitted. The interface layers are thought of as mainly comprising matrix material between the plies and hence again, the constitutive model for the interface layers differs from that in Section 4.1 in only one respect. The plasticity model is identical to that in Section 4.1, but the elasticity model is modified such that we take $E_f = E_m$ in the interface layers. Thus, in-plane pressure dependent shear yielding is permitted in the interface layers. The need to include the pressure dependence of the shear yielding necessitates the approach of modelling the interface between the plies as a layer of finite thickness with all stress components present rather than as a conventional cohesive surface; see Remmers et al. (2013) for a discussion on pressure dependent cohesive models. In all simulations presented subsequently this modified model is employed with $h_i = 0.04h$. All other model details including boundary conditions and material properties remain as specified above.

Predictions of the nominal stress versus strain response for the compression of the $L = 10$ mm specimen are included in Fig. 15b along with predictions of the full model with mesh size $e = h/12$: we argue that the reduced model approximates the converged solutions of the full model.

4.5. Predictions of the reduced model

Predictions of the compressive stress versus strain of the SPC060 grade for specimen sizes in the range $5 \text{ mm} \leq L \leq 10 \text{ mm}$ are plotted in Fig. 16. Recall that no failure is included in the FE model, and the calculations were terminated at an applied strain $\varepsilon_n = 0.18$. The specimen sizes chosen here correspond to the measurements included in Fig. 6b. The FE predictions have an initial elastic response followed by a reduction in the slope $d\sigma_n/d\varepsilon_n$ due to the onset of plasticity. However, the corresponding measurements plotted in Fig. 6b have a slightly concave initial slope due to compaction of the initial voids within the specimen (recall Fig. 8): this effect is not included

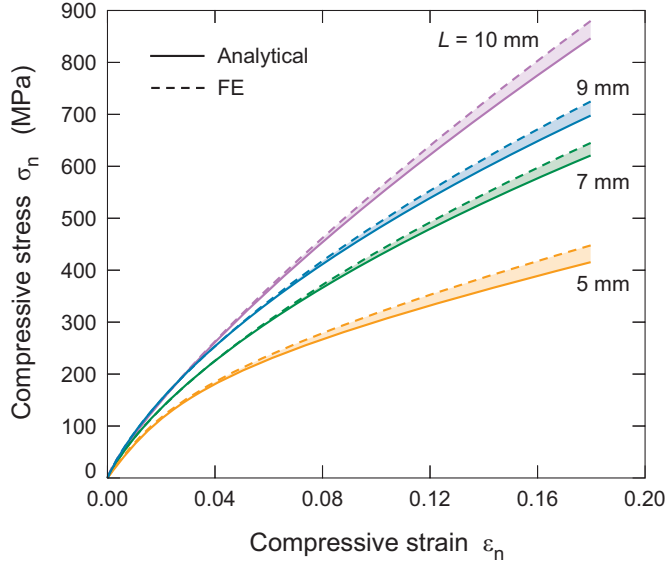


Figure 16: Comparison between predictions of the σ_n versus ε_n responses of the SPC060 composite using the reduced FE and analytical models. Results are shown for the specimen sizes corresponding to the measurements in Fig. 6b.

in the FE model and hence the predicted and measured stress versus strain curves are qualitatively different. However, we shall show in Section 4.6 that the model still predicts the peak strength to a sufficient level of accuracy.

We proceed to use the FE predictions to illustrate the deformation mechanism that results in tensile fibre fracture during the out-of-plane compression of the $L = 8$ mm SPC060 specimens. For this application, it is convenient to define Σ as the average stress across a ply in the fibre direction, i.e.

$$\Sigma \equiv \frac{1}{h} \int_0^h \sigma_{11} dx_3 \quad (10)$$

where the subscripts refer to the local co-ordinate system. Predictions of the average stress Σ are plotted in Fig. 17a on the $X_1 = 0$ plane. Results are plotted for 5 levels of the applied nominal strain ε_n using the undeformed material co-ordinates such that $X_2 = L/2$ corresponds to the free edge of the ply while $X_2 = 0$ denotes the mid-point of the specimen. The stress Σ is tensile and rises steeply from zero at $X_2 = L/2$ and then asymptotes to a uniform value near the centre of the specimen. The level of the stress in this plateau regime increases with increasing ε_n but the stress within the steeply

rising regime is almost insensitive to the the value of the applied strain. Given that the tensile fibre stress increases from zero at the free surface towards the interior of the specimen suggests that “shear lag” is responsible for the generation of this tensile stress. In order to investigate this further, we plot in Fig. 17b contours of the displacement u_2 on the $X_1 = 0$ plane on the deformed FE meshes (deformations reduced by a factor of 2 and the fibre orientations sketched in the inset of the figure⁵). Plots are included in Fig. 17b for applied $\varepsilon_n=0.02$ and 0.18. We observe that the ply with fibres in the X_1 direction is extruded in the X_2 direction resulting in a high interfacial shear stress near the free surface of the specimen (i.e. near $X_2 = L/2$). This shear stress results in the build-up of a tensile fibre stress Σ in the ply with fibres in the X_2 direction: we shall use this insight to develop an analytical model for the compression of the Dyneema[®] specimens in Section 5.

The constitutive model presented here includes a pressure dependent shear strength. In order to investigate the effect of this pressure dependence we plot in Fig. 18a predictions of Σ for the $L = 9$ mm specimen at $\varepsilon_n = 0.1$ analogous to Fig. 17a but for three selected values of pressure sensitivity co-efficient μ (all other material parameters are held fixed at the reference values for the SPC060 grade). The corresponding predictions of the σ_n versus ε_n curves are included in Fig. 18b, also for the $L = 9$ mm specimen. It is clear from Fig. 18a that Σ builds up more slowly with decreasing μ and this results in a less stiff σ_n versus ε_n response (Fig. 18b).

4.6. Comparison between measurements and predictions of the peak strength

We proceed to use the FE simulations to predict the peak compressive strength of the Dyneema[®] specimens. The observations reported in Section 3 reveal that the peak strength is decided by tensile fracture of the fibres. Recall from Figs. 17a and 18a that the maximum fibre tensile stress Σ occurs in the interior of the specimen and increases with increasing ε_n . We stipulate that the peak compressive strength is achieved when the maximum value of Σ attains the tensile strength σ_f of a single UD ply in the fibre direction. This UD ply strength, for the different grades of Dyneema[®] investigated here, is taken as twice the peak tensile strength of the $[0^\circ/90^\circ]$ laminates;

⁵Note that only a single $[0^\circ/90^\circ]$ stack is analysed in the FE model but three such identical stacks are included to better illustrate the deformation mode in the specimen.

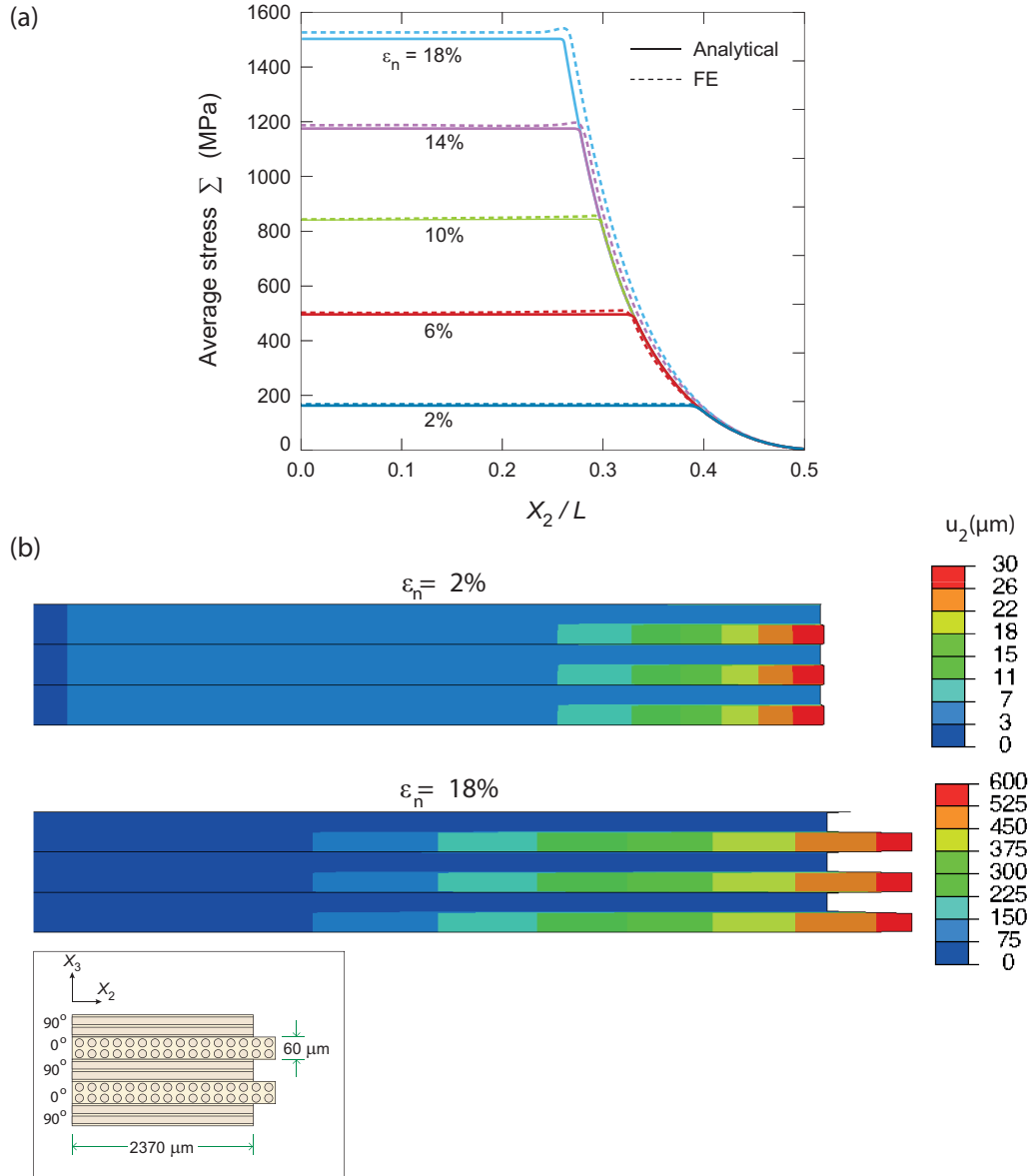


Figure 17: (a) Predictions of the reduced FE and analytical models of the spatial variation of Σ for the $L = 8$ mm SPC060 specimen on the $X_1 = 0$ plane. (b) FE predictions of the displacement u_2 on the $X_1 = 0$ plane plotted on the deformed FE mesh (deformations reduced by a factor of 2). Only a 2.37 mm edge section of the specimen is shown as sketched in the inset. In both (a) and (b) results are shown at select values of the applied strain ϵ_n .

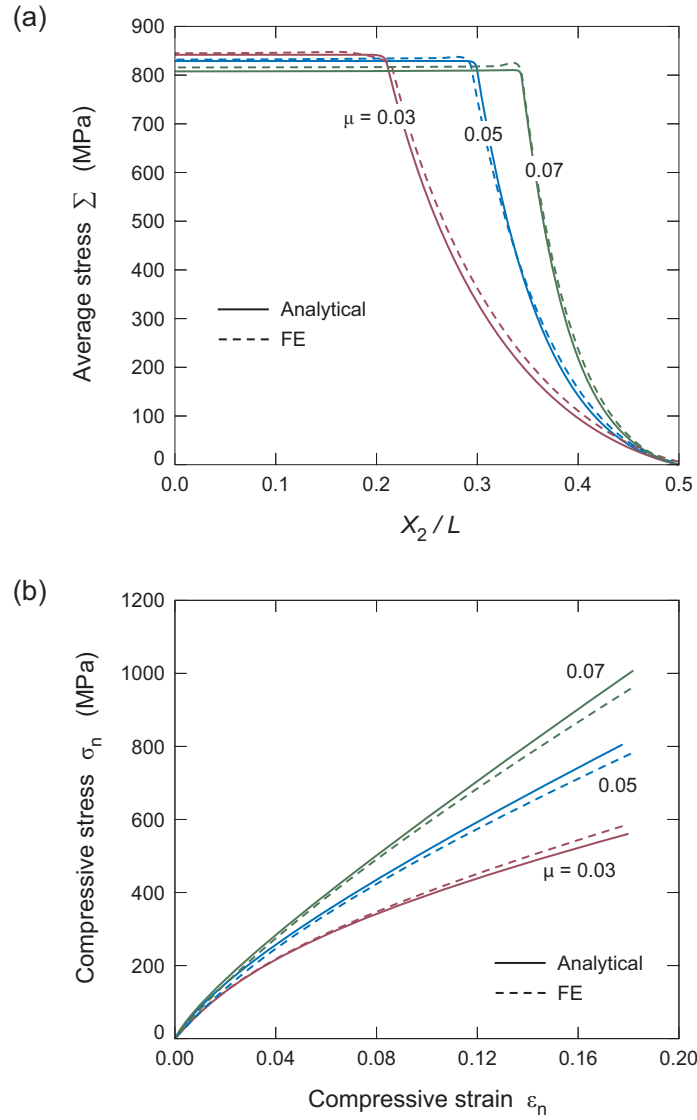


Figure 18: Predictions of the reduced FE and analytical models of (a) the spatial variation of Σ on the $X_1 = 0$ plane at an applied strain $\varepsilon_n = 0.1$ and (b) the corresponding σ_n versus ε_n responses. Results are shown for the $L = 9$ mm specimen for select values of μ and all other material parameters fixed at the values for the SPC060 composite.

recall Fig. 4a⁶.

Finite Element predictions of the peak compressive strength of the SPC060 grade are included in Fig. 10 as a function of the specimen size L for a range of values of μ (the only parameter that is not measured from independent tests). It is clear that the predicted peak strength increases with increasing μ . A comparison with the measured peak strength data, in Fig. 10, indicates that a value of $\mu \approx 0.05$ gives a good fit to the measurements. This value of μ is within the range reported for polymers, including PE (Ward, 1971). It follows that a relatively simple compression test can be used to extract the pressure sensitivity of the yield strength of Dyneema[®]. We note in passing that the predictions with $\mu < 0.02$ (i.e. low pressure sensitivity of the yield strength) predicted that no fibre fracture would occur for the specimen sizes investigated here and are not included in Fig. 10.

Finite Element simulations to determine the peak compressive strength of the other grades of Dyneema[®] composites were also conducted. The material parameters used for each of the grades are listed in Table 2: all parameters other than μ , E_m and G_{12} are extracted from the material tests and microstructural observations reported above in Section 2. The values of the shear and transverse ply moduli are reported by Liu et al. (2014). As for the SPC060 grade, a suitable value of μ was determined by fitting the FE predictions of the peak strength as a function of L to the measurements. The value of μ that gives the best agreement is listed in Table 2. The FE predictions using these parameters are included in Figs. 12 and 13 and show good agreement over the entire range of L investigated, with μ as the only fitting parameter. It is clear that μ does not vary greatly for the different grades of Dyneema[®]. We emphasise here that the value of μ as obtained by this procedure gives the pressure sensitivity of the shear strength of the composite, rather than just the matrix material. We anticipate that this pressure sensitivity might be similar to that of a granular material, i.e. to a large extent governed by the packing of the high volume fraction of fibres in the composite similar to the way in which the pressure sensitivity of the shear strength of a granular material depends on the packing of granular particles. The micro-mechanical origins of the pressure sensitivity of Dyneema[®] are

⁶Recall that $[0^\circ/90^\circ]$ laminates have equal volume fractions of 0° and 90° plies. The assumption that the UD strength is twice the strength of these laminates then follows from the assumption that the load carrying capacity of the 90° plies is negligible compared to that in the 0° plies in these tensile tests.

Material Property	SPC060	SSC060	SPC120	SPC030	XSC060
UD laminate failure stress σ_f (MPa)	1600	1600	1600	1600	1760
Shear strength τ_o (MPa)	2	0.5	2	2	0.5
Ply thickness h (μm)	60	60	120	30	60
Transverse ply modulus E_m (GPa)	10	10	10	10	10
Ply modulus in fibre direction E_f (GPa)	80	80	80	80	80
Shear Modulus G_{12} (GPa)	3	3	3	3	3
Pressure sensitivity coefficient μ	0.05	0.05	0.05	0.05	0.07

Table 2: The material properties and geometrical parameters used in the FE and analytical predictions of the responses of the six composite grades investigated in this study.

beyond the scope of this study.

While FE predictions of the compressive response of the UD grade are not explicitly included here for the sake of brevity, we note in passing that the compressive response of the UD composite is a direct input to the constitutive model developed here. Thus, the model specifies the compressive true stress versus strain response of the UD composite to be elastic ideally-plastic with a compressive yield strength equal to $2\tau_o$.

5. Shear lag analysis

We present an analytical model for the out-of-plane compressive response of the $0^\circ - 90^\circ$ Dyneema[®] composites, motivated by the FE analysis reported above. The FE analysis (see Figs. 17 and 18a) suggests that (i) there is a

central region over which there is a spatially uniform state of stress and (ii) a boundary regime around the periphery of the specimen within which the fibre stress increases towards the interior of the specimen via the development of a shear lag zone. Based on this understanding we develop models for each of these regions and then proceed to connect them.

Consider the specimen as sketched in Fig. 5 such that the specimen lies in the $X_1 - X_2$ plane with the compression direction along X_3 . We develop the analysis using this co-ordinate system, so the stresses and strains are in this global co-ordinate system rather than the local co-ordinate system x_i wherein the fibres always lie in the x_1 direction. Also, unless otherwise specified, we analyse a ply whose fibres lie along the X_1 direction so that a stress and strain σ_{11} and ε_{11} , respectively in the global co-ordinate system refers to a fibre stress and strain, respectively.

The FE analysis discussed in the previous section has demonstrated that while the stresses within a ply vary in the X_1 and X_2 directions, the direct stresses σ_{11} , σ_{22} and σ_{33} are reasonably uniform through the thickness of the ply. Thus, in the analytical model developed below, we shall *a-priori* assume that these stresses are uniform through the thickness of the ply, which simplifies the analysis considerably.

5.1. Analysis of a specimen of infinite extent

We first present an analysis of the compressive response of a specimen of infinite dimensions in the $X_1 - X_2$ plane, i.e. $L \rightarrow \infty$. In this specimen all effects due to the traction-free edges of the specimen can be neglected and the specimen will have a spatially uniform stress and strain state within each ply. We shall subsequently show that this analysis also holds in the central section of finite specimens.

Recall that the specimen is compressed in the X_3 direction with tractions $T_1 = 0$ on $X_1 = c_1$, and $T_2 = 0$ on $X_2 = c_2$, where c_1 and c_2 are arbitrary constants. Additionally, the alternating 0° and 90° plies (of equal thickness) will have the same stress and strain state, albeit rotated through 90° about the X_3 axis. It follows from equilibrium considerations that the stress state in the ply under consideration is constrained such that $\sigma_{11} = -\sigma_{22}$ and the ply strains $\varepsilon_{11} = \varepsilon_{22}$. First consider elastic straining with no plasticity. With the above constraints on the stresses and strains, the elastic constitutive relation (3) specifies that σ_{11} and σ_{33} are related:

$$\sigma_{33} = -\sigma_{11} \frac{1}{\nu} \left(\frac{E_f + E_m}{E_f} \right), \quad (11a)$$

where we have taken $\nu_{12} = \nu_{21} = 0$ and written $\nu_{23} = \nu$. The elastic stress versus strain relations in terms of the applied σ_{33} are given as

$$\varepsilon_{11} = \varepsilon_{22} = -\frac{\nu\sigma_{33}}{E_f + E_m}, \quad \text{and} \quad (11b)$$

$$\varepsilon_{33} = \frac{\sigma_{33}}{E_m} \left[1 - \frac{\nu^2 E_f}{E_m + E_f} \right]. \quad (11c)$$

We proceed to determine the stress state at which yield first occurs and then analyse the subsequent elastic-plastic response. As the state of stress is spatially uniform, all shear stresses vanish. The only active yield criterion is Eq. (4a) and it then follows that, for an actively yielding ply under a compressive applied σ_{33} (recall compressive stresses are negative) with $|\sigma_{33}| > |\sigma_{22}|$

$$\sigma_{33} = -\frac{1}{1 - \mu} [\sigma_{11}(1 + \mu) + 2\tau_0]. \quad (12)$$

The plastic strain ε_{22}^p is given by

$$\varepsilon_{22}^p = \varepsilon_{22} - \varepsilon_{22}^e, \quad (13)$$

where $\varepsilon_{22} = \varepsilon_{11} = \sigma_{11}/E_f$ for all values of σ_{11} as we assume that straining in the x_1 direction is always purely elastic. The elastic strain ε_{22}^e follows from (3) as

$$\varepsilon_{22}^e = -\frac{\sigma_{11}}{E_m} - \nu \frac{\sigma_{33}}{E_m}. \quad (14)$$

Substituting for σ_{33} in terms of σ_{11} from (12) and setting $\varepsilon_{22}^p = 0$ in Eq. (13) stipulates that at the onset of yielding the stress in the fibre direction equals

$$\sigma_{11}^Y = \frac{2\tau_0\nu}{(1 - \mu) \left[\left(1 + \frac{E_m}{E_f}\right) - \nu \left(\frac{1 + \mu}{1 - \mu}\right) \right]}, \quad (15)$$

and the the applied stress at the onset of yield follows from Eq. (12) as

$$\sigma_{33}^Y = -\frac{2\tau_0}{1 - \mu} \left[1 + \frac{\nu}{\left[\left(1 + \frac{E_m}{E_f}\right) \left(\frac{1 - \mu}{1 + \mu}\right) - \nu \right]} \right]. \quad (16)$$

In order to determine the post-yield stress versus strain response, we note that plastic compressibility implies that $\varepsilon_{22}^p = -\varepsilon_{33}^p$ as $\varepsilon_{11}^p = 0$. For a stress $\sigma_{11} \geq \sigma_{11}^Y$, the stress σ_{11} versus strain ε_{33} relation then follows as

$$\varepsilon_{33} = -\frac{\sigma_{11}}{E_f} \left[1 + 2\frac{E_f}{E_m} \left(\frac{1-\nu}{1-\mu} \right) \right] - \frac{2\tau_0(1-\nu)}{E_m(1-\mu)}. \quad (17)$$

In summary, the compressive stress versus strain relation of the specimen of infinite extent is given by

$$\varepsilon_{33} = \begin{cases} \frac{\sigma_{33}}{E_m} \left[1 - \frac{\nu^2 E_f}{E_m + E_f} \right] & \text{for } \sigma_{33}^Y \leq \sigma_{33} \leq 0, \\ \frac{\sigma_{33}(1-\mu) + 2\tau_0}{E_f(1+\mu)} \left[1 + 2\frac{E_f}{E_m} \left(\frac{1-\nu}{1-\mu} \right) \right] & \\ -\frac{2\tau_0(1-\nu)}{E_m(1-\mu)} & \text{for } \sigma_{33} < \sigma_{33}^Y. \end{cases} \quad (18)$$

The peak value of σ_{33} denoted as σ_{\max}^∞ is attained when the stress σ_{11} reaches the failure strength σ_f of a UD ply in the fibre direction. Upon noting that the stress $\sigma_{11}^Y \approx \tau_0 \ll \sigma_f$, it is clear that fibre failure and the peak compressive strength of the composite is only attained after plasticity initiates in the composite. Thus, the peak strength σ_{\max}^∞ is given by setting the stress σ_{11} equal to the the ply tensile failure stress σ_f in Eq. (12), i.e.

$$\sigma_{\max}^\infty = -\frac{1}{1-\mu} [\sigma_f(1+\mu) + 2\tau_0]. \quad (19)$$

5.2. Shear lag analysis for the peripheral region around the specimen

The above analysis of the infinite specimen neglected the shear lag boundary layer that forms around the specimen's periphery and results in the build-up of tensile fibre stresses towards the interior of the specimen. In this section we present a simple shear lag analysis for this boundary layer. The moduli mismatch between the 0° and 90° plies implies that the elastic solution for the interfacial stress between the two plies is singular at the specimen surface $X_1 = L/2$. Thus, we anticipate that the plasticity initiates at the edge of the specimen immediately upon loading and it suffices to neglect elasticity within this boundary layer.

Within the boundary layer, the shear stresses do not vanish and the yield criteria f_1 , f_3 and f_4 in Eq. (4) are active. Now consider a section of the

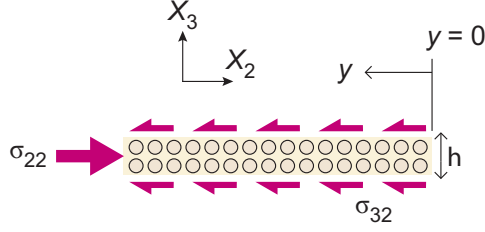


Figure 19: Sketch of the free-body diagram of a ply on the $X_1 = 0$ plane with fibres in the X_1 direction. The sketch includes the global co-ordinate system and the definition of the local co-ordinate y .

specimen on the plane $X_1 = 0$ and define the co-ordinate $y = L/2 - X_2$ as shown in Fig. 19 such that $y = 0$ is the free-edge of the specimen at $X_2 = L/2$ and $y = L/2$ is at the center of the specimen. Recalling that $\sigma_{11} = -\sigma_{22}$ the yield criteria f_1 and f_3 reduce to

$$\sigma_{33} = -\frac{1}{1-\mu} [-\sigma_{22}(1+\mu) + 2\tau_0], \quad \text{and} \quad (20a)$$

$$\sigma_{32} = \tau_0 + \frac{\mu}{1-\mu} [-\sigma_{22} + \tau_0]. \quad (20b)$$

Recall that we assume that the stress σ_{22} to be uniform through the thickness the ply. Equilibrium in the X_2 direction then dictates

$$h \frac{\partial \sigma_{22}}{\partial y} = -2\sigma_{32} \quad (21)$$

Substituting for σ_{32} from Eq. (20b) and integrating using the boundary condition $\sigma_{22} = 0$ at $y = 0$ gives

$$\sigma_{11} = -\sigma_{22} = \frac{\tau_0}{\mu} \left[\exp\left(\frac{ay}{h}\right) - 1 \right], \quad (22)$$

where $a \equiv 2\mu/(1-\mu)$. The corresponding stress σ_{33} within this shear lag zone is obtained by substituting for σ_{11} from Eq. (12) in Eq. (22) and is given by

$$\sigma_{33} = -\frac{(1+\mu)\tau_0(e^{ay/h} - 1) + 2\tau_0\mu}{\mu(1-\mu)}. \quad (23)$$

Setting the stress σ_{11} equal to the tensile failure stress σ_f in Eq. (22) gives the width of the shear lag zone y_f at failure as

$$y_f = h \frac{1-\mu}{2\mu} \ln \left(1 + \frac{\mu\sigma_f}{\tau_0} \right). \quad (24)$$

For the pressure insensitive case of $\mu = 0$, the shear lag zone size scales linearly with the strength ratio σ_f/τ_0 according to $y_f/h = 0.5\sigma_f/\tau_0$. However, for finite μ the dependence of y_f/h on σ_f/τ_0 is significantly weaker due to the logarithmic term in Eq. (24).

5.3. Overall compressive response of a finite specimen

We proceed to derive expressions for the overall stress versus strain response for the out-of-plane compression of a square specimen of side L . At any given applied nominal strain ε_n , we assume that there is a shear lag layer of size y_s along the periphery of the specimen and the remaining central square portion of side $L - 2y_s$ has vanishing shear tractions as described by the equations derived in Section 5.1.

The relevant expressions are considerably simplified when presented in parametric form in terms of the stress $r = \sigma_{11}$ in the fibre direction within the central section of the specimen. Hence we proceed with deriving relations for the nominal stress σ_n and nominal strain ε_n in terms of r . Two regimes of the response emerge from the above analysis: (i) for small values of σ_n the central portion of the specimen deforms elastically and (ii) at higher applied loads the entire specimen plastically deforms. In both cases the specimen deforms plastically within the shear lag region.

First, consider the compressive force sustained by the portion of the specimen within the shear lag regime y_s . The compressive force F_s is obtained by integrating Eq. (23) such that

$$F_s = -2L \left\{ 1 + \left(\frac{L - 2y_s}{L} \right) \right\} \int_0^{y_s} \left[\frac{(1 + \mu)\tau_0(e^{ay/h} - 1) + 2\tau_0\mu}{\mu(1 - \mu)} \right] dy, \quad (25a)$$

where y_s is given in terms of r from Eq. (22) as

$$y_s = h \frac{1 - \mu}{2\mu} \ln \left(1 + \frac{\mu r}{\tau_0} \right). \quad (25b)$$

The compressive stresses within the central section of side $L - 2y_s$ are constant and thus the applied nominal stress σ_n is obtained from the weighted average

$$\sigma_n = -\frac{F_s}{L^2} - \left(1 - 2\frac{y_s}{L} \right)^2 \sigma_c \quad (26)$$

where σ_c is the compressive stress in the X_3 direction in the central section and given by Eqs. (11a) and (12) for the elastic and plastic regimes,

respectively. With $r \equiv \sigma_{11}$, Eq. (15) specifies the value of r at which the deformation transitions from elastic to plastic and thus the nominal stress is given in terms of r as

$$\sigma_n = \begin{cases} r \left(1 - \frac{2y_s}{L}\right)^2 \frac{E_m}{\nu} \left(\frac{1}{E_m} + \frac{1}{E_f}\right) \\ + \frac{4y_s\tau_0}{L\mu} \left(1 - \frac{y_s}{L}\right) \left[\left(\frac{e^{ay_s/h} - 1}{ay_s/h}\right) \left(\frac{1+\mu}{1-\mu}\right) - 1\right] & \text{for } r \leq \sigma_{11}^Y \\ \left(1 - \frac{2y_s}{L}\right)^2 \left[r \left(\frac{1+\mu}{1-\mu}\right) + \frac{2\tau_0}{1-\mu}\right] \\ + \frac{4y_s\tau_0}{L\mu} \left(1 - \frac{y_s}{L}\right) \left[\left(\frac{e^{ay_s/h} - 1}{ay_s/h}\right) \left(\frac{1+\mu}{1-\mu}\right) - 1\right] & \text{for } r \geq \sigma_{11}^Y. \end{cases} \quad (27a)$$

The relation between the applied strain ε_n and r is given by the analysis of the Section 5.1 such that

$$\varepsilon_n = \begin{cases} \frac{r}{E_m} \left[\frac{E_m}{\nu} \left(\frac{1}{E_m} + \frac{1}{E_f}\right) - \nu\right] & \text{for } r \leq \sigma_{11}^Y \\ \frac{r}{E_f} \left[1 + 2\frac{E_f}{E_m} \left(\frac{1-\nu}{1-\mu}\right)\right] + \frac{2\tau_0(1-\nu)}{E_m(1-\mu)} & \text{for } r \geq \sigma_{11}^Y. \end{cases} \quad (27b)$$

Equation (27) gives the overall σ_n versus ε_n relation in parametric form in terms of the stress r .

The peak value of σ_n is attained when the fibre stress $r = \sigma_f$. As discussed above in Section 5.1 for Dyneema[®] composites $\sigma_f \gg \sigma_{11}^Y$ and hence it suffices to only consider the plastic branch as given by Eq. (27a)₂. Setting $r = \sigma_f$ we obtain the compressive peak strength of the specimen as

$$\sigma_{\max} = \left(1 - 2\frac{y_f}{L}\right)^2 \left[\sigma_f \left(\frac{1+\mu}{1-\mu}\right) + \frac{2\tau_0}{1-\mu}\right] \\ + \frac{4y_f\tau_0}{L\mu} \left(1 - \frac{y_f}{L}\right) \left[\left(\frac{e^{ay_f/h} - 1}{ay_f/h}\right) \left(\frac{1+\mu}{1-\mu}\right) - 1\right], \quad (28)$$

where y_f is the shear lag length at failure as given by Eq. (24). It follows that for $y_f > L/2$ the fibre stress never attains its failure value of σ_f and the specimen deforms plastically without attaining a peak stress. This second regime was observed in the experiments on the SPC060 specimens of length

$L < 4$ mm; recall Section 3 . In the other extreme of $L \rightarrow \infty$, the predicted peak strength asymptotes to the value $\sigma_{\max} \rightarrow \sigma_{\max}^{\infty}$ as given by Eq. (19). It is worth noting that for the practical case of $\sigma_f \gg \tau_0$, the asymptotic strength of the composite is predominantly governed by the tensile strength σ_f and depends very weakly upon the shear strength τ_0 .

5.4. Comparison with FE predictions and measurements

We first present comparisons between the above analytical model and the FE predictions of Sections 4.5 and 4.6. The analytical predictions of the overall σ_n versus ε_n responses for the SPC060 grade are included in Fig. 16 using the reference material parameters. Similar to the FE model predictions in Fig. 16 no failure is analysed in this case. Over the range of specimen sizes and strains considered the analytical and FE predictions are in excellent agreement. Next, consider the spatial variation of the fibre stress Σ as plotted in Figs. 17a and 18a. Substituting for σ_{33}^Y from Eq. (16) in Eq. (18) gives the strain at which plasticity first initiates in the central region as

$$\varepsilon_n^Y = \frac{2\tau_0\nu}{(E_f + E_m)(1 - \mu) - \nu E_f(1 + \mu)} \left[\frac{E_f(1 - \nu^2) + E_m}{\nu E_m} \right]. \quad (29)$$

The fibre stress Σ then follows from the analysis of Sections 5.1 and 5.2 as

$$\Sigma(X_2) = \begin{cases} \min \left[\frac{\nu E_m E_f \varepsilon_n}{E_f(1 - \nu^2) + E_m}, \frac{\tau_0}{\mu} \{e^{a/h(L/2-X_2)} - 1\} \right] & \text{for } \varepsilon_n \leq \varepsilon_n^Y \\ \min \left[\frac{[\varepsilon_n E_m(1 + \mu) - 2\tau_0(1 - \nu)] E_f}{E_m(1 - \mu) + 2E_f(1 - \nu)}, \frac{\tau_0}{\mu} \{e^{a/h(L/2-X_2)} - 1\} \right] & \text{otherwise.} \end{cases} \quad (30)$$

Analytical predictions of Σ are included in Figs. 17a and 18a along with the FE results as discussed in Section 4.5. Further, Figs. 10, 12 and 13 include analytical predictions (material properties listed in Table 2) of σ_{\max} for $L \geq 2y_f$ for all the different grades of Dyneema[®] composites investigated here. In all cases, the analytical and FE predictions are in excellent agreement and both the FE and analytical models predict the measured values of σ_{\max} to an adequate level of accuracy. In fact, as shown in the Appendix there is some scatter in the measurements due to material variability and the predictions lie within this measurement variability.

6. Concluding remarks

The out-of-plane compressive response of Dyneema[®] composites was measured for six composite grades with varying fibre and matrix strength, ply thickness and ply lay-ups. Out-of-plane compression of composites with a $[0^\circ/90^\circ]$ lay-up resulted in the build-up of tensile fibre stresses which led to catastrophic failure of the specimens when the fibre failure strength was attained. The peak strengths of these composites increased with increasing in-plane specimen dimensions, and fibre and matrix strength, but decreased with increasing ply thickness. By contrast, no fibre tensile stresses were generated during the compression of the uni-directional composites. Instead, these specimens compressed plastically at an imposed stress on the order of the matrix shear strength. X-ray tomography combined with measurements of the pressure distribution over the loaded face of the specimen demonstrated that the indirect tension generated in the $[0^\circ/90^\circ]$ composites was due to the development of a shear-lag regime around the periphery of the specimens. The shearing of the Dyneema[®] composites within this regime under the applied pressure is the basis for extraction of the pressure sensitivity of the composites' shear strength.

A constitutive model is proposed for the individual plies of Dyneema[®] composites with a pressure dependent shear strength. The out-of-plane compressive response of the $[0^\circ/90^\circ]$ composites is then calculated using the Finite Element (FE) method. The pressure sensitivity of the shear strength is estimated by comparing the measurements of the compressive response with these predictions. An analytical shear-lag model for this response is also developed. Predictions of the analytical model are in excellent agreement with both the FE simulations and the measurements for all the composite grades investigated here. The analytical model thus provides simple closed-form expressions for determining the pressure sensitivity of Dyneema[®] composites from measurements of the compressive strength as a function of specimen size.

We have demonstrated that compression of the widely used $[0^\circ/90^\circ]$ Dyneema[®] composites results in the generation of an indirect tensile stress within the fibres of the composite. Such a compressive stress state is expected to be generated immediately under a projectile during the ballistic impact of a Dyneema[®] composite, as studied by Karthikeyan et al. (2013b) and O'Masta et al. (2013). Dynamic failure by the generation of this indirect tension was first hypothesised by Woodward et al. (1994) but largely ignored in the lit-

erature as numerical models did not reveal this mechanism. However, these numerical studies typically employed a homogenised continuum description of the Dyneema[®] composite: the prediction of the indirect tension mechanism requires the cross-ply architecture to be explicitly accounted for. The implications of the indirect tension failure mechanism on the ballistic response of Dyneema[®] composites remains a topic for future study.

Appendix: Variability in the measured values of the peak strengths

Measurements of the peak strength σ_{\max} of the SPC060 and SSC060 grades are plotted in Fig. A.1 as a function of the specimen size L . At least 10 nominally identical tests were conducted in each case and the error bars in Fig. A.1 indicate the variability in the measurements, with the high and low values corresponding to the absolute maximum and minimum values recorded, while the circles and squares show the mean values of the measurements for the SPC060 and SSC060 grades, respectively. It is clear that the scatter/variability in the measurements increases with increasing specimen size. The analytical predictions of σ_{\max} are also included in Fig. A.1 using the material properties listed in Table 2. It is clear that the Dyneema[®] composites have significant material variability, presumably due to manufacturing defects such as void distributions, fibre waviness, variability in fibre strength etc. However, the trends in the measurement are clear, i.e. (i) the compressive strength of the composites increases with increasing L and (ii) the SPC060 grade is stronger compared to the SSC060 grade over the range of specimen sizes investigated in this study.

Acknowledgements

The work was funded by the Defence Advanced Research Projects Agency (DARPA) under grant number W91CRB-11-1-0005. We are grateful to DSM for providing the Dyneema[®] composites used in this study, and specifically to Dr. Harm van der Werff and Dr. Ulrich Heisserer for their help and advice.

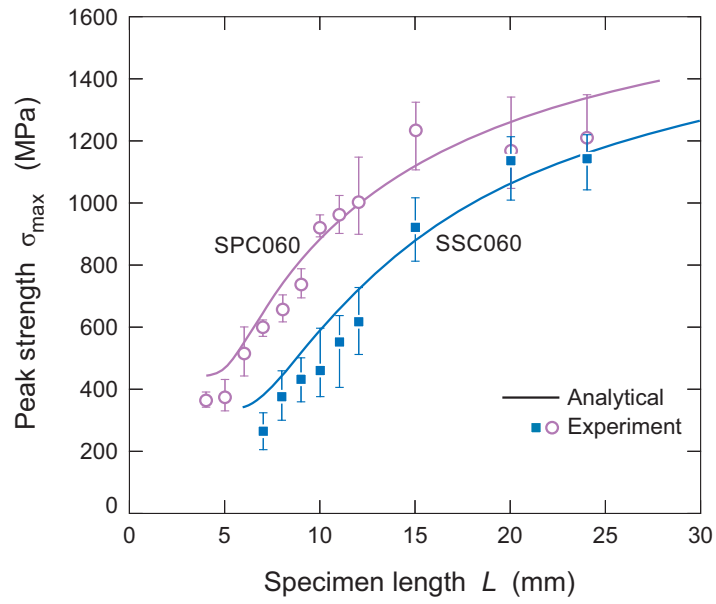


Figure A.1: Measurements and analytical predictions of the peak strength σ_{\max} as a function of the specimen size L of the SPC060 and SSC060 composite grades. At least 10 repeat measurements were conducted and the error bars in the plots show the variation in the measurements along with the mean values.

References

- Benloulou, I. C., Rodriguez, J., Martinez, M., Galvez, V., 1997. Dynamic tensile testing of aramid and polyethylene fiber composites. *International Journal of Impact Engineering* 19, 135–146.
- Cunniff, P. M., 1999. Dimensionless parameters for optimization of textile-based body armor systems. In: Reinecke, W. G. (Ed.), *Proceedings of the 18th International Symposium on Ballistics*. Technomic Publishing Company Inc., Lancaster PA, San Antonio, TX, USA, pp. 1303–1310.
- Govaert, L., Lenstra, P. J., 1992. Deformation behavior of oriented UHMW-PE fibers. *Colloid and Polymer Science* 270, 455–464.
- Greenhalgh, E., Bloodworth, V. M., Iannucci, L., Pope, D., 2013. Fractographic observations on dyneema composites under ballistic impact. *Composites Part A* 44, 51–62.
- Grujicic, M., Arakere, G., He, T., Bell, W., Glomski, P., Cheeseman, B., 2009. Multi-scale ballistic material modeling of cross-ply compliant composites. *Composites Part B* 40, 468–482.
- Henriksson, A., 1990. Transverse compressive behaviour of carbon-epoxy laminates and its influence on contact laws. Master's thesis, The Aeronautical Research Institute of Sweden, Stockholm, Sweden.
- Iannucci, L., Pope, D., 2011. High velocity impact and armour design. *Express Polymer Letters* 5, 262–272.
- Karthikeyan, K., Russell, B. P., Fleck, N. A., O'Masta, M. R., Wadley, H. N. G., Deshpande, V. S., 2013a. The soft impact response of composite laminate beams. *International Journal of Impact Engineering* 60, 24–36.
- Karthikeyan, K., Russell, B. P., Fleck, N. A., Wadley, H. N. G., Deshpande, V. S., 2013b. The effect of shear strength on the impact response of laminated composite plates. *European Journal of Mechanics A: Solids* 42, 35–53.
- Koh, A., Shim, V., Tan, V., 2010. Dynamic behaviour of UHMWPE yarns and addressing impedance mismatch effects of specimen clamps. *International Journal of Impact Engineering* 37, 324–332.

- Koiter, W. T., 1953. Stress-strain relations, uniqueness and variational theorems for elastic-plastic materials with a singular yield surface. *Quarterly of Applied Mathematics* 11, 350–354.
- Liu, G., Thouless, M. D., Deshpande, V. S., Fleck, N. A., 2014. Collapse of a composite beam made from ultra high molecular-weight polyethylene fibres. *Journal of the Mechanics and Physics of Solids* 63, 320–335.
- O’Masta, M. R., Deshpande, V. S., Wadley, H. N. G., 2013. Mechanisms of projectile penetration in dyneema composite structures. *International Journal of Impact Engineering* To appear.
- Phoenix, S. L., Porwal, P. K., 2003. A new membrane model for the ballistic impact response and V50 performance of multi-ply fibrous systems. *International Journal of Solids and Structures* 40, 6723–6765.
- Remmers, J. J. C., de Borst, R., Verhoosel, C. V., Needleman, A., 2013. The cohesive band model: a cohesive surface formulation with stress triaxiality. *International Journal of Fracture* 181, 177–188.
- Russell, B. P., Karthikeyan, K., Deshpande, V. S., Fleck, N. A., 2013. The high strain rate response of ultra high molecular-weight polyethylene: from fibre to laminate. *International Journal of Impact Engineering* 60, 1–9.
- Smith, P., Lemstra, P. J., 1980. Ultra-high-strength polyethylene filaments by solution spinning/drawing. *Journal of Materials Science* 15, 505–514.
- Smith, P., Lemstra, P. J., Kalb, B., Pennings, A. J., 1979. Ultra high-strength polyethylene filaments by solution spinning and hot drawing. *Polymer Bulletin* 1, 733–736.
- Ward, I. M., 1971. Review: The yield behaviour of polymers. *Journal of Materials Science* 6, 1397–1417.
- Wilding, M. A., Ward, I. M., 1978. Tensile creep and recovery in ultra-high modulus linear polyethylenes. *Polymer* 19, 969–976.
- Woodward, R. L., Egglestone, G. T., Baxter, B. J., Challis, K., 1994. Resistance to penetration and compression of fibre-reinforced composite materials. *Composite Engineering* 4, 329–341.